

Computation of Weakly-Compressible Highly-Viscous Polymeric Liquid Flows

M. F. Webster ^{1*}, I. J. Keshtiban ², and F. Belblidia ¹

⁽¹⁾ Institute of Non-Newtonian Fluid Mechanics,
Department of Computer Science,
University of Wales, Swansea, SA2 8PP, UK.

⁽²⁾ Research visitor, Tarbiat Modares University of Teheran, Iran.

* Author for correspondence. Email: M.F.Webster@Swansea.ac.uk

Abstract

We introduce a high-resolution time-marching pressure-correction algorithm to accommodate weakly-compressible highly-viscous polymeric liquid flows at low Mach number. As the incompressible limit is approached ($Ma \approx 0$), the consistency of the compressible scheme is highlighted in recovering equivalent incompressible solutions. In the viscous-dominated regime of low Reynolds number (zone of interest), the algorithm treats the viscous part of the equations in a semi-implicit form. Two discrete representations are proposed to interpolate density: a piecewise-constant form with gradient recovery and a linear interpolation form, akin to that on pressure. Numerical performance is considered on a number of classical benchmark problems for viscous polymeric liquid flows to highlight consistency, accuracy and stability properties. Validation bears out the high quality of performance of both compressible flow implementations, at low to vanishing Mach number. Neither linear, nor constant density interpolations schemes degrade the second-order accuracy of the original incompressible fractional-staged pressure-correction scheme. The piecewise-constant interpolation scheme is advocated strongly as the preferred method of choice, with its advantages of order retention, yet efficiency in implementation.

Key Words: Finite element, pressure-correction, highly-viscous, polymeric-liquid, compressible flow, low Mach number.

1. INTRODUCTION

This article addresses the need to predict solutions for weakly-compressible highly-viscous polymeric liquid flows, with attention to both accuracy and efficiency. The approach commences from a framework adopted for incompressible flow and viscoelastic fluids, upon which compressibility is grafted. Here, viscous Newtonian fluids are considered, so that inertial effects are low to moderate, yet viscosities may be high. In such a context, the level of corresponding Reynolds number is low (typically, $Re \approx O(1)$), diffusion dominates and convection terms may be resolved without difficulty. This lies in contrast to the aerodynamic high-convection regime (inertial, low-viscosity, high-speed), which gives rise to shocks and where characteristic-based methods are relevant. Here, such issues do not emerge. Furthermore, our ultimate goal is to address *viscoelastic flows*, where convection of stress (fluid-memory) is important, that does demand a suitable form of upwinding, see Petrov-Galerkin forms (Matallah *et al.*, 1998).

Compressibility effects occur in both liquids and gases through the variation of density. Density itself, depends on temperature, pressure and concentration levels. Flows of liquid materials, at moderate pressure levels, can be considered as incompressible. Nevertheless, at large pressure-differences, such flows may display some mild compressibility effects. Mach number, the ratio of fluid velocity to the speed of sound ($Ma = u/c$), characterises the influence of compressibility on a flow field. Flows at low Mach number may be described as incompressible, whilst for those at moderate to high Mach number, compressibility effects will be prominent. The incompressible limit of a compressible flow is approached, under suitable constraints, as Mach number vanishes (Munz *et al.*, 2003). Under such circumstances, the speed of sound is much larger than the velocity of the liquid, resulting in fast pressure waves, where rapid pressure equalization takes place.

Low Mach number flows play an important role, occurring widely in nature and industrial processes. Circulation within the oceans is driven mainly by density gradients, which arise via variation of salinity and temperature. Common human bodily functions, such as, singing, weaseling, breathing and talking, all represent examples of low Mach number flow regimes. In addition, some industrial gas flow configurations take place at low Mach number. Free convection and combustion are yet further examples, where flow occurs driven under the variation of density with temperature. Compressibility has some impact upon applications such as in: liquid impact, jet cutting and liquid impact erosion, in steam turbine for example (Kelmanson and Maunder, 1999, Field, 1999); polymer extrusion (Georgiou, 2003); injection molding with polymer melts (Han and Im, 1997); recovery and exploration of petroleum (Wu and Pruess, 2000). Compressibility should be incorporated in order to rigorously investigate such phenomena as cavitation (Brujan, 1999), instabilities (Georgiou, 2003), and shrinkage and warpage (Han and Im, 1997), liquid impact erosion (Kelmanson and Maunder, 1999, Jackson and Field, 1999). Moreover, in capillary rheometry, compressibility may have a significant influence on features such as the time-dependent pressure changes within a system (see piston-driven flows, Ranganathan *et al.*, 1999)

Much attention has been devoted towards the computational solution of flows that manifest compressibility effects. Today, sophisticated numerical solvers can handle high Reynolds number compressible flow computations. To solve such scenarios, different methodologies have emerged under finite element and finite volume approaches. Within finite elements, this gives rise to various Streamline-Upwind/Petrov-Galerkin (SUPG) algorithms, with stabilization techniques such as Galerkin Least-Square (GLS) (Hughes *et al.*, 1989). Equivalently, in the finite volume context, some high-performance counterpart algorithms have emerged (Moukalled and Darwish, 2001, Karki and Patankar, 1989,

Karimian and Schneider, 1995). Nonetheless, Wong *et al.* (2001), state that some SUPG compressible-based algorithms may fail to yield adequate numerical solutions for flows that approach the incompressible limit. Degradation in the solution has been observed in several studies (Turkel *et al.*, 1997, Wong *et al.*, 2001). One of the key difficulties in constructing numerical methods to address weakly-compressible flows arises from the fact that the governing equations switch type. The equations for viscous compressible flow form a hyperbolic-parabolic system with finite waves-speeds (inviscid case, hyperbolic), whilst those for incompressible viscous flow assume an elliptic-parabolic system with infinite wave propagation rates (for viscoelastic regimes, a sub-system of hyperbolic form may augment the whole). In addition, the compressible equations for low Mach number may be associated with large disparity between the acoustic wave-speed, $(u + c)$, and the entropy wave convected at the fluid-speed, (u) (Wong *et al.*, 2001, Turkel *et al.*, 1997, Jenny and Muller, 1999). Here, the condition number for the equation system is related to the reciprocal of the Mach number.

In the present article under algorithmic development, we restrict ourselves to *Newtonian viscous polymeric liquid flows under isothermal conditions* and where Reynolds and Mach numbers are generally low (viscoelastic alternatives to follow). An equation of state is applied to represent density variation with pressure. To this end the well-established Tait model (Tait, 1888) is suitably extended, chosen on physical ground to represent polymeric materials (Huang and Chow, 1974, Han and Im, 1997). Key modifications to handle weakly-compressible flows, introduced within our fractional-staged incompressible pressure-correction algorithm, are related primarily to the finite element representation of density. Two types of interpolation are employed: first, a *piecewise-constant* form (incompressible per element), with a nodal recovery for density gradients (second-stage); second, a *linear interpolation* form, akin to that employed for the pressure field. We

demonstrate that these modifications do not degrade second-order accuracy of the original pressure-correction scheme. We illustrate how the algorithm can handle weakly-compressible highly-viscous flow at low Mach number, as well as incompressible flows (hence, zero Mach number configurations).

The present article is organized as follows: background theory is introduced in Section 2. The governing equations for compressible viscous flows are expounded in Section 3. In Section 4, we introduce the equation stages in the scheme, followed in Section 5 by the finite element (FE) discretisation adopted. In Section 6, we present the application of our methodology to several benchmark test-problems, including driven-cavity flows, channel flows and contraction flows. Scheme variants are validated for consistency via mesh refinement, to extract respective orders of accuracy. Comparison, is made against incompressible counterparts and the literature, complementing the high-order of accuracy achieved. This proves itself above second-order for smooth flows. The piecewise-constant interpolation scheme is advocated strongly on a number of counts, as outlined below.

2. BACKGROUND THEORY

The need for algorithmic developments to handle the low Mach number flow regime may be justified on a number of grounds. For example, there are many natural phenomena, where accurate simulation in this scenario is demanded. In some instances, flow problems may exhibit mixed-type (compressible/incompressible), where some sections of the flow are incompressible with locally low Mach number, whilst other zones are significantly compressible. Under such circumstances, if the incompressible region is sufficiently small, compared to the compressible section, there is little loss of accuracy when incompressibility is neglected. However, there are flow regimes, such as in aerodynamics (high-speed/low-viscosity), where large regions of low Mach number coexist alongside

supersonic flow regions. This arises in aerofoil high angle-of-attack configurations, where the solution will degrade if based solely on a compressible description. In addition, in some material processing instances, such as for polymers during the filling stage of injection moulding and in extrusion, there are some locally compressible regions, whilst most of the flow remains incompressible. Therefore, it is both desirable and necessary to develop algorithms that can handle both regimes, concurrently. From a numerical perspective, conventional approaches to handle low Mach number flows can be subjugated into two main categories: *density-based* schemes and *pressure-based* schemes (Moukalled and Darwish, 2001, Karki and Patankar, 1989). We proceed to follow the latter, upon which the present article is based.

Density-based methods represent a large class of schemes adopted for compressible flows (for more details see, Keshtiban *et al.*, 2003). Turkel *et al.* (1997) and Guillard and Viozat (1999) have identified that, in the low Mach number limit, the discretised solution of the compressible flow equations may fail to provide an accurate approximation to the incompressible equations (quoting Guillard and Viozat (1999) in particular). As a ‘rule-of-thumb’, compressible schemes without modification become impractical for Mach numbers lower than around 0.3 (Roller and Munz, 2000). In contrast, pressure-based methods were originally conceived to solve incompressible flows, adopting pressure as a primary variable. With this approach, pressure variation remains finite, irrespective of Mach number, rendering computation tractable throughout the entire spectrum of Mach number (Karki and Patankar, 1989), hence circumventing the shortcomings of density-based methods. The first implementation of pressure-based schemes for compressible flow is widely attributed to the early contribution of Harlow and Amsden (1968), based on a semi-implicit finite difference algorithm.

Pressure-correction, or projection methods, are pressure-based fractional-staged schemes with correction for velocity and pressure (see Peyret and Taylor, 1983), introduced through the pioneering work of Chorin (1968) and Temam (1969). Such methods have been employed effectively within several finite volume implementations, say through the SIMPLE (Semi-Implicit Pressure Linked Equations) family of schemes (Patankar, 1980). Karki and Patankar (1989) developed the SIMPLER method for compressible flows, applicable for a wide range of problem-speeds. These SIMPLE methods are first-order in time. Munz *et al.* (2003) extended the SIMPLE scheme for low Mach number flow employing multiple pressure variables, each being associated with different physical response. Similar procedures have been adopted by others (Bijl and Wesseling, 1998, Mary *et al.*, 2000, Roller and Munz, 2000). Pressure-correction was taken forward within finite differences to a second-order by Van Kan (1986). Alternatively, within finite elements, Donea *et al.* (1982) introduced a pressure-correction fractional-step method, designed to significantly reduce computational overheads in transient incompressible viscous flow situations. Similarly, Zienkiewicz *et al.* (1995) have introduced the characteristic-based-split procedure (CBS). This implementation is a Taylor-Galerkin/Pressure-Correction scheme, suitable for both incompressible and compressible flow regimes. The crux here, is to split the equation system into two parts: a part of convection-diffusion type (discretised via a characteristic-Galerkin procedure) and one of self-adjoint type. With the characteristic-based-split scheme, one may solve both parts of the system in an explicit manner. Alternatively, one may use a semi-implicit scheme for the first part, allowing for much larger time-steps, and solve the second part implicitly, with its advantage of unconditional stability. The characteristic-based-split procedure has been tested successfully on a number of scenarios, for example, transonic

and supersonic flows, low Mach number flows with low and high viscosity, and in addition, on shallow-water wave problems.

In the incompressible viscoelastic regime, computational methods have matured significantly over the last two decades or so (Saramito and Piau, 1994, Guénette and Fortin, 1995, Baaijens, 1998, Walters and Webster, 2003). Here, it is desirable to extend the methodology into the weakly-compressible regime, and particularly so for viscous polymeric liquid flows. In this regard, density-based preconditioning or asymptotic methods (see Keshtiban *et al.*, 2003) often demand significant recoding. On the other hand, extending an existing incompressible flow code to accommodate compressibility would appear somewhat more straightforward. This is the thesis and starting point adopted for implementation throughout the current study. Precisely, our aim is to modify a pressure-correction technique for incompressible polymeric flows to accommodate weakly-compressible, yet highly-viscous, flows under low Mach number configurations. This presents a natural extension to our earlier incompressible flow studies for viscous (Hawken *et al.*, 1990), inelastic (Ding *et al.*, 1995, three-dimensional) and viscoelastic (Matallah *et al.*, 1998, Wapperom and Webster, 1998) fluids, where we have developed a hybrid schema to attain second-order accuracy.

3. GOVERNING EQUATIONS

The conservation of mass and momentum transport equations employed in the simulation of compressible steady Newtonian fluid under isothermal conditions may be considered as:

$$\frac{\partial \rho}{\partial t} + \nabla \cdot (\rho u) = 0 \quad (1)$$

$$\rho \frac{\partial u}{\partial t} = [\nabla \cdot \tau - \rho u \cdot \nabla u - \nabla p] \quad (2)$$

where independent variables are (t,x) , time and space, and dependent field variables are ρ , u , τ , p , density, velocity, stress and pressure, respectively. Stress is related to the kinematic field through a constitutive law, which is defined for compressible Newtonian

$$\text{fluids as: } \tau_{ij} = \mu \left(d_{ij} - \frac{2}{3} (\nabla \cdot u) \delta_{ij} \right) \quad (3)$$

where μ is the viscosity, δ_{ij} is the Kronecker delta tensor and $2d = \nabla u + \nabla u^T$ is the rate of deformation tensor (here, superscript T denotes tensor transpose).

To extract non-dimensionalised governing equations, we define the following scales on physical variables as: velocity U_o , dimension L , density ρ_o , pressure and stress $\left(\frac{\mu U_o}{L} \right)$ and time $\frac{L}{U_o}$. We introduce the dimensionless group Reynolds number, $\text{Re} = \frac{\rho_o U_o L}{\mu}$, to

extract the non-dimensionalised momentum equation:

$$\text{Re } \rho \frac{\partial u}{\partial t} = \nabla \cdot \tau - \text{Re } \rho u \cdot \nabla u - \nabla p. \quad (4)$$

Correspondence in the continuity equation provides:

$$\frac{\partial \rho}{\partial t} + \nabla \cdot (\rho u) = 0. \quad (5)$$

To complete the set of governing equations, it is necessary to introduce an equation of state relating density to pressure. For polymeric liquids, we consider the modified Tait equation of state (Tait, 1888), in the form

$$\frac{p + B}{p_o + B} = \left(\frac{\rho}{\rho_o} \right)^m, \quad (6)$$

where, m and B are parameters and p_o , ρ_o denote reference values for pressure and density, respectively. This empirical equation of state is suitable for dense materials, such as polymer melts and solutions, water and other liquids (Huang and Chow, 1974, under

linear approximation ($m=1$), see also, Ranganathan *et al.*, 1999, and Georgiou, 2003). Note, that strictly speaking, this equation applies only to isentropic change. Nevertheless, it can be utilised with reasonable accuracy in more general instances, since m and B are independent of entropy and ρ_o is constant (Brujan, 1999). We follow Karki and Patankar (1989), Zienkiewicz *et al.* (1995) and Brujan (1999), and after differentiating the equation of state, we gather:

$$\frac{\partial P}{\partial \rho} = mk\rho^{m-1} = \frac{m(p+B)}{\rho} = c_{(x,t)}^2 \quad (7)$$

where $k = \frac{(p_o + B)}{\rho_o^m}$ is a constant and $c_{(x,t)}$ is the derived speed of sound, a field parameter distributed in space x and time t . Other alternative assumptions may be adopted, such as isenthalpic (Lien and Leschziner, 1993) or homenthalpic (Munz *et al.*, 2003). Note, under steady-state conditions, temporal pressure change will vanish and the steady solution will be independent of the above stated assumptions. However, this may affect transient results and convergence properties of the associated schemes. The next step is to incorporate the above theory within a discrete representation.

4. PRESSURE-CORRECTION SCHEME - COMPRESSIBLE FLOWS

Recently, we have advocated various advances in the application of our incompressible second-order, fractional-staged, time-marching pressure-correction procedures. This has accommodated model to complex flows exemplified through free-surface flows (Ngamaramvaranggul and Webster, 2000a), wire-coating (Ngamaramvaranggul and Webster, 2000b) and dough mixing applications (Baloch *et al.*, 2002). Our present goal is to elaborate the constructive steps to incorporate weak-compressibility upon such a

formulation, where we have polymeric liquid flow applications firmly in mind (viscous form, viscoelastic to follow).

The base formulation-framework is that of a pressure-correction scheme, split into three distinct, fractional-stages. Briefly, at a first stage, which is divided into two sub-stages, the momentum equation is employed to predict the velocity field at a half-stage. Subsequently, the momentum equation is employed to compute the velocity (u^*) at a full-step (two-step Lax-Wendroff style, Taylor-Galerkin phase, (Löhner *et al.*, 1984). The second stage (pressure-correction) utilises the continuity equation to evaluate a temporal pressure-difference, inserting the approximate velocity field (auxiliary variable, u^* , computed at stage one). Crank-Nicolson averaged treatment for diffusion/source term introduces *semi-implicitness* to the stages and overcomes restrictive diffusive stability limitations. At a third stage, the end-of-step velocity field (u^{n+1}) is corrected, based upon the pressure-difference on the time-step, derived at the second stage. One may draw distinction to the characteristic-based-split procedure of Zienkiewicz *et al.* (1995), in the retention of pressure gradients, within the representation of the momentum equation over stage one. This ensures solution at stage two for temporal pressure increments, delivering second-order accuracy to the system and aiding the appropriate setting of boundary conditions throughout. The characteristic-based-split approach, alternatively, conveys the pressure gradient term to the third fractional-staged equation for velocity-correction.

To extend the incompressible algorithm to deal with compressible flows, one must first appreciate the key role that pressure plays in a compressible flow. In the low Mach number limit, where density is almost constant, the role of pressure is to influence velocity through the continuity equation, so that conservation of mass is satisfied (Moukalled and Darwish, 2001). Indeed, in this instance, density and pressure are only weakly-linked variables. To recast the above incompressible scheme into one appropriate for weakly-

compressible highly-viscous flows, we follow the ideas of Karki and Patankar (1989) and Zienkiewicz *et al.* (1995). Here, the temporal derivative of density from the continuity equation is replaced by its equivalent in pressure, appealing to an equation of state. To observe this, we take the equation that defines the auxiliary variable (u^*):

$$u^{n+1} = u^* - \left(\frac{\Delta t}{\rho} \right) \theta \nabla (\Delta p^{n+1}), \quad (8)$$

with constant scheme factor $0 \leq \theta \leq 1$ and operator $\Delta(\cdot)^\theta = (\cdot)^\theta - (\cdot)^n$. Here, θ is normally taken as 0.5 for second order accuracy, as below. By taking the divergence of this equation, one gathers:

$$\nabla \cdot (\rho u^{n+1}) = \nabla \cdot (\rho u^*) - \Delta t \theta \nabla^2 (\Delta p^{n+1}), \quad (9)$$

from which, by appealing to the compressible form of the continuity equation, one may insert the discrete temporal derivative of density:

$$\frac{\Delta \rho^{n+1}}{\Delta t} + \nabla \cdot (\rho u^*) = \Delta t \theta \nabla^2 (\Delta p^{n+1}). \quad (10)$$

In addition, by employing the chain rule upon $\frac{\partial P}{\partial \rho}$ of Eq.(7) and taking difference quotients, we may relate density temporal increment to pressure increment through,

$$\frac{\Delta \rho^{n+1}}{\Delta t} = \frac{1}{c_{(x,t)}^2} \frac{\Delta p^{n+1}}{\Delta t}. \quad (11)$$

Finally, we substitute Eq.(11) into Eq.(10) to realise a compressible form of the temporal evolutionary expression for pressure:

$$\frac{1}{c_{(x,t)}^2} \frac{\Delta p^{n+1}}{\Delta t} - \Delta t \theta \nabla^2 (\Delta p^{n+1}) = -\nabla \cdot (\rho u^*). \quad (12)$$

This is the new stage 2 equation, introduced to provide the compressible pressure-correction formulation (see below).

5. FINITE ELEMENT DISCRETIZATION

The momentum and mass conservation equations are discretised via the FE method. Based on a triangular mesh, the velocity vector $u(x,t)$, and pressure $p(x,t)$ are taken over elements as:

$$u(x,t) = U_j(t) \phi_j(x), \quad j=1,6 \text{ and } p(x,t) = P_k(t) \psi_k(x), \quad k=1,3 \quad (13)$$

where $\phi(x)$ represents continuous quadratic polynomial interpolation, $\psi(x)$ piecewise-linear interpolation, and time-dependent nodal velocity and pressure vectors are U and P , respectively. We note in the context of highly-viscous polymeric flows, velocity gradients are a dominant feature and their accurate prediction, via higher-order levels of interpolation on velocity, are a well-established characteristic of such scenarios. For density interpolation, two types of interpolation are considered: piecewise-constant over an element, with recovery for the gradient of density, and piecewise-linear interpolation (as for the pressure field). The semi-implicit discretised equations for the compressible pressure-correction scheme may be expressed in three fractional stages:

$$\textit{Stage 1a:} \quad \left[\frac{M_\rho}{\Delta t / 2} + \frac{1}{2} S_U \right] \left(\Delta U^{n+\frac{1}{2}} \right) = -[S_U U + N_\rho(U)U - L^T P]^n \quad (14)$$

$$\textit{Stage 1b:} \quad \left[\frac{M_\rho}{\Delta t} + \frac{1}{2} S_U \right] (\Delta U^*) = -[S_U U - L^T P]^n - [N_\rho(U)U]^{n+\frac{1}{2}} \quad (15)$$

$$\textit{Stage 2:} \quad \left[\frac{M_C}{\Delta t^2} + \theta K \right] (\Delta P^{n+1}) = -\frac{1}{\Delta t} L^T U^* \quad (16)$$

$$\textit{Stage 3:} \quad \frac{1}{\Delta t} M_\rho (U^{n+1} - U^*) = \theta L^T \Delta P^{n+1} \quad (17)$$

where, in the case of a planar coordinate system, matrix notation implies:

$$(M_\rho)_{ij} = \int_{\Omega} \rho \phi_i \phi_j d\Omega \quad (18)$$

$$(N_\rho)_{ij} = \int_{\Omega} \rho \phi_i (U \cdot \nabla \phi_j) d\Omega \quad (19)$$

$$(K)_{ij} = \int_{\Omega} \nabla \psi_i \cdot \nabla \psi_j d\Omega \quad (20)$$

$$(L_k)_{ij} = \int_{\Omega} \psi_i (\nabla \cdot \phi_j)_k d\Omega \quad (21)$$

$$(S_U)_{ij} = (S_{lm})_{ij}, \quad l, m = 1, 2 \quad (22)$$

$$(S_{11})_{ij} = \int_{\Omega} \mu \left(2 \frac{\partial \phi_i}{\partial x} \cdot \frac{\partial \phi_j}{\partial x} + \frac{\partial \phi_i}{\partial y} \cdot \frac{\partial \phi_j}{\partial y} - \frac{2}{3} \frac{\partial \phi_i}{\partial x} \cdot \frac{\partial \phi_j}{\partial x} \right) d\Omega \quad (23)$$

$$(S_{12})_{ij} = \int_{\Omega} \mu \frac{\partial \phi_i}{\partial y} \cdot \frac{\partial \phi_j}{\partial x} d\Omega \quad (24)$$

$$(S_{22})_{ij} = \int_{\Omega} \mu \left(\frac{\partial \phi_i}{\partial x} \cdot \frac{\partial \phi_j}{\partial x} + 2 \frac{\partial \phi_i}{\partial y} \cdot \frac{\partial \phi_j}{\partial y} - \frac{2}{3} \frac{\partial \phi_i}{\partial y} \cdot \frac{\partial \phi_j}{\partial y} \right) d\Omega \quad (25)$$

$$(M_c)_{ij} = \int_{\Omega} \frac{\psi_i \psi_j}{c^2(x,t)} d\Omega \quad (26)$$

$$(L_k^\rho)_{ij} = \int_{\Omega} \psi_i \left\{ \nabla \rho \phi_j + \rho \frac{\partial \phi_j}{\partial x_k} \right\} d\Omega. \quad (27)$$

These matrices, with their corresponding integrals, may be evaluated analytically or via quadrature on each triangular control element (say, seven point Gauss quadrature rule). Note, that in expression (27) for (L_k^ρ) matrix, when a compressible approach is employed based on a piecewise-constant density interpolation, the element interior contribution of the first term forming the density-gradient representation will vanish. To remedy this position during matrix evaluation at stage 2, a corner nodal density value is assigned, so that equivalent to linear interpolation may be recovered, leading to piecewise-constant

gradients. An element averaging (recovery) technique is adequate for this purpose (Matallah *et al.*, 1998). From a computational point of view, matrix evaluation is three-times quicker with ρ -constant than linear, with most work being required for the convection matrix of expression (19). Note also, that solution of each fractional-staged equation is attained via an iterative preconditioned Jacobi solver, that is, with exception of the temporal pressure-difference equation, which is solved through a direct Choleski procedure (Baloch *et al.*, 2002). The major difference between the forms of the incompressible and compressible algorithm lies in stage-2. For compressible instances, density becomes a distributed variable. The incompressible variant emerges, when density is a constant throughout the solution domain and the speed of sound approaches infinity.

6. NUMERICAL EXAMPLES

To calibrate the algorithm, we consider three numerical examples, regarded as benchmarks in the viscous/viscoelastic regime of interest. Here, we use the time-marching procedures to extract steady-state solutions. The first example is a driven cavity problem, simulated here to qualify the accuracy of the algorithms in a complex re-circulating flow. A second example concerns a channel flow problem introduced to demonstrate the consistency of the method in simulating weakly-compressible flow. For these two examples, a Cartesian coordinate system is employed. A third example is a contraction flow problem, used in both planar and axisymmetric configuration and for a range of compressible flow settings to investigate variation in Tait model parameters. For density interpolation, both piecewise-constant and linear forms are introduced. In all instances, the fluid is considered to be Newtonian and the flow to be laminar. Dimensionless time steps are adopted, satisfying a local Courant condition constraint and convergence to a steady-

state is monitored, via a relative temporal increment L_2 norm on the solution, taken to a tolerance of $O(10^{-8})$ (see Hawken *et al.*, 1990).

6.1. Cavity flow

Commonly, this problem is utilized as a standard incompressible flow benchmark for evaluating stability and accuracy of numerical schemes (Peyret and Taylor, 1983, Hawken *et al.*, 1990, Ghia *et al.*, 1982). Flow is enclosed (closed streamlines) and specified within a unit square cavity, where the fluid is driven by the upper-plate (lid) at a given velocity. The problem is characterised by the Reynolds number (Re), with velocity-scale, U , the lid-velocity, and length-scale, h , the height of the cavity. Two cases, with different driving lid-velocity profiles, are considered: case (a) with a variable profile of type $U = 16x^2(1-x)^2$, leading to a continuous solution. This case is well-documented in Hawken *et al.* (1990) and Peyret and Taylor (1983) references. Case (b) is one of conventional constant profile form, widely reported in the literature, which possesses singularity in the solution at the cavity top-corners.

First, validation is sought for the incompressible algorithm, being conducted for $Re=100$ and $Re=400$, as standard problem parameters. In Figure 1, contour patterns for pressure and stream function are plotted based on case (b) with a regular mesh of 40×40 square sub-divisions, each split into two triangular elements. The contour results reflect those shown in Zienkiewicz *et al.* (1995), Ghia *et al.* (1982), Peyret and Taylor (1983) and Hawken *et al.* (1990). Pressure level lines illustrate, maxima (P_A) is at the downstream lid-corner and minima at the upstream corner (P_B). The stream function contours display the recirculating nature of the flow, with distortion near the singular corners, and a secondary Moffatt-type vortex in the lower right-corner. Streamlines are twisted and distorted with increase of convection (Re) towards the downstream corner, and the primary vortex centre

drops within the cavity. Stream function vortex centre values (S_+) and (S_*) are also indicated. Figure 2 presents the computed incompressible velocity components along the vertical and horizontal centerlines for $Re=100$ and $Re=400$. The results are contrasted against those of Ghia *et al.* (1982), revealing close agreement and providing confidence in the level of accuracy achieved for incompressible solutions. This position is also reflected in solutions at $Re=1$, see Hawken *et al.* (1990).

For compressible flow under case (b) condition and $Re=100$, the two parameters employed in the Tait state equation are fixed as $(m,B)=(2,300)$, leading to $Ma\approx 0.03$ and 21% density increase above the incompressible state. In Figure 3, Mach number contours are provided for piecewise-constant density interpolation (with recovery of the gradients). The figure exhibits the singularity in the solution through the distortion in the Mach number contours near the cavity top corners. In addition, pressure and streamline contour patterns practically replicate those observed under the incompressible regime, and hence are not reproduced for the compressible case.

Accuracy is assessed via the infinity norm, ($\|E_h\|_\infty$), on the longitudinal velocity, a maximum norm of the difference from the fine mesh solution, scaled by the maximum of all normed values. This is conducted, based on two types of density interpolation (piecewise-constant with recovery of gradients and linear with constant gradients) under $Re=100$. Both variable and constant lid-velocity profiles are investigated. Due to the lack of an analytical solution, a fine mesh solution on 40×40 is taken as reference, against which three further mesh solutions are compared (5×5 , 10×10 and 20×20). Nodal values on both cavity centerlines ($X=0.5$ and $Y=0.5$) are sampled for the computation of $\|E_h\|_\infty$. Figure 4a presents the pattern of behaviour in the infinite velocity error norm, with respect to mesh-size reduction for case (a), variable lid-profile, and $Re=100$. Similar data are reported for case (b), constant lid-profile, in Figure 4b. For the smooth solution (case a),

the order of accuracy for the three different implementations is above 2.5, approaching a third-order. This order of accuracy has been achieved in some of our earlier work for incompressible viscoelastic flows (Wapperom and Webster, 1998). For case (b), where the solution presents singularities, the order is around 1.4. This is in keeping with expectation, being well known that the presence of singularities in a problem will result in a decline in accuracy (Hawken *et al.*, 1990). Note, the same behaviour in error norm is detected in both case (a) and (b), and for the three algorithmic implementations. This confirms that modifications incorporated within the initial incompressible algorithm, to accommodate weakly-compressible flows, do not degrade the accuracy of the pressure-correction method itself.

Assessment of time-convergence to steady-state has been performed on case (b), based on a 5x5 mesh and a time-step of $\Delta t=0.01$, with initial conditions assigned as quiescent (see Webster and Townsend (1990) for tracking of true transient solutions). Histories of the relative error norms in velocity ($E^l(U)$) and pressure ($E^l(P)$) are provided in Figure 5 for the three algorithmic variants. The results reflect a superior rate of convergence for the two compressible algorithm forms, as compared to that for the incompressible algorithm: 30% less time-steps are required for the compressible implementation to reach an equitable level of tolerance (order of convergence is $(O(2.6))$ for compressible as compared to $(O(2.4))$ for incompressible forms). This we attribute to the improvement in system matrix condition number, brought about via introduction of the mass-matrix, M_c and right-hand-side adjustment via L_k^ρ at stage 2 (see Eq.16). As a consequence, larger time-steps may be selected within the compressible regime, as opposed to the incompressible alternative. Note, the same rate of time-stepping convergence is observed in both compressible algorithmic implementations.

6.2. Planar channel flow

Specification for the channel flow problem is provided in Figure 6a. For viscous-dominated liquid flows, this problem is a useful reference point. For incompressible flows, an analytical solution is available, being devoid of complex geometric influence, displaying one-dimensional shear-flow patterns. The compressible low Mach number equivalent, provides quantitative reference data to be compared against its incompressible counterpart. Here, inflow/outflow boundary conditions must be specified. The channel dimensions are taken as two units long by one unit wide. No-slip boundary conditions are assumed on solid boundaries. At flow-entry we consider a parabolic flow profile for the longitudinal velocity U_X , with maxima in U_X imposed as unity. Cross-sectional component U_Y vanishes at both entry and exit. At the outlet, the longitudinal velocity (U_X) remains unspecified (natural condition) and a reference pressure is fixed as zero. The Reynolds number is considered as unity and compressibility Tait parameters (m, B), are assigned as (2,100), to manifest influence of compressibility ($Ma \approx 0.08$ and 8% density elevated above the incompressible state). Again, a time-step of $\Delta t = 0.01$ is found suitable.

We begin by assessing the mass balance for this problem from inlet to outlet, via satisfaction of the continuity equation. Results, based on three levels of regular mesh refinement (rectangular sub-divisions split into triangles) and flow regime, are presented in Table I. The error in the difference between flow entering and leaving the channel is realised as $O(0.1\%)$ and less on the finer mesh, demonstrating conservation of mass overall.

Velocity and Mach number field solutions in Figures 6 and 7 are presented with: top figures for mesh 10×10 , middle for 20×20 mesh and bottom 40×40 mesh. Quantification of the different algorithmic variants (incompressible, compressible linear) are conveyed through separate columns. Figure 6 presents the U_X -velocity contours. To illustrate the

adjustment of velocity along the channel, solution values are in-laid at coordinate sample locations are selected of $(X=0.0, 1.0, 2.0)$, $(Y=0.125, 0.50, 0.75)$, as depicted in Figure 6a. U_x -velocity contours are parallel to the flow in the incompressible regime, where the velocity profile is parabolic. In either of the piecewise-constant or linear density interpolation instances (only one shown), the flattening of velocity profile is more pronounced and the smoothness of contours is improved by increasing mesh density. The fact that velocity contours are not parallel reflects the convective nature of the flow. In addition, for both piecewise-constant and linear interpolation representations correspondence is close curved flow-speed compensates so as to satisfy mass conservation at the outlet. This explains why, under equitable conditions, the outlet flow-speed is higher in the compressible regime, as compared to that for incompressible flow.

Figure 7 presents corresponding Mach number contours (with in-laid solution values). Note that, the speed of sound is infinite for an incompressible liquid, resulting in a vanishing Mach number. Since density is related to pressure through the equation of state, linked via the speed of sound, the Mach number reflects the relationship between velocity and pressure. Thus, for piecewise-constant and linear density interpolation, the differences observed in Mach number may be attributed to variation in pressure and velocity. In addition, these results demonstrate the ability of the compressible implementations to deal with low Mach number situations ($Ma < 8 \cdot 10^{-2}$). Here, we observe yet again, a reasonable correspondence between results for either density interpolation option (2% difference on finest mesh).

Table II presents the values of the pressure and density along the centreline of the channel at different X-locations ($X=0.0, 0.5, 1.0, 1.5, 2.0$) for the different implementations and mesh size. Contours of pressure are level-lines across the flow cross-section. For incompressible flow and with a mesh size $10 \cdot 10$, we recover the exact solution reflecting a

nondimensional inlet-outlet pressure-drop of 16 units. For compressible flow, with either piecewise-constant or linear density interpolation, the pressure-drop is slightly elevated over incompressible flow and increases with mesh-density (5% increase on the finest mesh). In addition, with mesh size 40*40, we begin to detect departure in pressure profiles contours from linear form (slightly parabolic). Note that for density, here results for the incompressible liquid are suppressed, as density remains at a constant level. Compressibility effects are apparent, with the density of the fluid entering the channel being larger (by about 8% for both density representations) than that departing. As with pressure, density contours degrade slightly from linear structure span-wise across the flow. Since density at the inlet is larger, the flow-rate is greater in the compressible (piecewise-constant or linear interpolation) as compared to the incompressible case. This explains the reported corresponding elevation in pressure-drop of above.

6.3. Contraction flow

In the third benchmark, we introduce a more complex test problem typical of industrial setting and with a view to viscoelastic computations to follow. This consists of a contraction flow under both planar and axisymmetric reference, see Figure 8a. Here, we observe larger pressure-drops than in straight channel flow above, and the effects of compressibility are significant. The total length of the channel is taken as 76.5 units and the contraction ratio is four to one. For this test problem, boundary conditions follow as specified for the channel flow problem above, with a Reynolds number set to unity.

6.3.1. Planar contraction flow

a) Mesh refinement: First, mesh refinement is conducted, based on a multi-block meshing strategy to discretized the half-contraction channel-geometry, with conformal

mapping in each sub-block and matching of boundary nodes at interfaces. In this manner, three different meshes M1, M2 and M3 with different levels of refinement have been constructed, see Figure 8b-d with characteristics quantified in Table III, where details are recorded for total numbers of elements, nodes, degree of freedom, corner mesh density and minimum element size (see Matallah *et al.* (1998)). We have need to define a temporal relative-increment L_2 -norm to govern time-stepping convergence history as:

$$E^t(X) = \frac{\|X^{n+1} - X^n\|_2}{1 + \|X^{n+1}\|_2}. \quad (28)$$

Plots for temporal convergence history to steady-state on pressure ($E^t(P)$) and velocity ($E^t(U)$) are displayed in Figure 9, under the planar coordinate system. This covers the three different meshes and algorithmic variants, with Tait parameters set to $(m,B)=(5,3000)$, resulting in $Ma \approx 0.04$ and 4% density variation above the incompressible state, and a time-step of $\Delta t = 0.05$. One may observe that both compressible implementations follow practically identical trends, and that oncemore, as in the channel flow problem, convergence rates are improved by approximately 30% over the incompressible form. As one suppresses oscillations in temporal velocity increments through mesh refinement, one also controls the oscillatory evolutionary patterns for time-increments in pressure. This is anticipated, since convergence-history in pressure is constrained in a Lyapunov norm, see Van Kan (1986). On pressure, for the three meshes considered, we observe high-frequency/low-amplitude oscillations for the incompressible implementation compared to the compressible counterpart (low-frequency/large-amplitude).

Figure 10 illustrates pressure and stream function fields, with their associated contour levels, for the three meshes. Here, only piecewise-constant density interpolation results are illustrated. In Table IV, values of pressure, velocity components (U_x, U_y) and vortex information are given at the contraction plane (sample location highlighted by a cross ‘+’

in Figure 8a). Note, for the same compressibility setting, the piecewise-constant and the linear density interpolations deliver identical results (differing by less than 0.025%) for a particular mesh size (linear form suppressed). The associated contour plots are observed to smooth with refinement. Note, that mesh M2 is felt adequate for detailed coverage below, as this mesh is able to highlight the salient corner vortex and is computationally cost-effective compared to the finest mesh M3.

b) Solutions at $(m,B)=(2,300)$: Increasing compressible effects, via $(m,B)=(2,300)$, leads to $Ma \approx 0.3$. Here, there is variation in density above incompressible by about 65%, exaggerated to highlight the difference between density representations. Figure 11, on mesh M2, illustrates the adjustment across the density field for linear density interpolation, and those in Mach number between piecewise-constant and linear density interpolations around the contraction zone. Solutions point values for velocity, pressure, density and Mach number are presented in tabular form (Table Va) at the sampled spatial locations (a,b,c,d) of Figure 8d. In the pressure field, for instance, we observe about 1.5% difference between both compressible representations. Generally, solution values at the sampled locations are larger for compressible above incompressible flow (by about 25% in pressure elevation). That is with the exception of X-velocity component (U_X) at the location c, where the flow slows down in the compressible case just prior to the contraction plane. One notes that compressible conditions lead to conservation of mass-flow-rate in contrast to volume-flow-rate for incompressible flows. In Mach number, contour field plots (Figure 11) reflect some differences (by about 9% at c-location), according to the choice of density interpolation employed. This is because the Mach number is related to the speed of sound, which itself is linked directly to density, via the Tait equation. Hence, the level of density

interpolation comes into play. One may observe, under piecewise-constant density interpolation, Mach number contours are less-smooth over elements of larger size.

Figure 12 presents solution profiles for different variables (X-velocity, pressure, density and Mach number) at the contraction channel centreline for both compressible interpolation variants. The results provide clear evidence that low-order density interpolation with gradient recovery, is able to reproduce results comparable to those with linear density interpolation. Near the exit, a discrepancy of about 20%, at this level of Mach number, is observed in Mach number, with those for constant density interpolation being higher than those for the linear alternative. This departure is due mainly to the adjustment in both velocity and pressure across the exit zone, and to some degree to the mesh quality there.

6.3.2. *Circular contraction flow*

Under an axisymmetric frame of reference, pressure-differences exceed those for the planar equivalent. Here, Tait parameters are set to $(m,B)=(5,3000)$, leading to mild compressible influences ($Ma\approx 0.16$, density elevated 17% above the incompressible state). First, as above for planar flow, we confirm that similar trends are observed in field variables based on both form of density interpolation (see Figures 13). Profiles over the contraction channel centreline follow the planar case (as in Figure 12). Sampled solutions values for the different variables are presented in Table Vb at the selected spatial locations of Figure 8d. Oncemore, similar results are observed for both compressible representations around this contraction zone (less than 0.1% in pressure). There is about 8% pressure elevation in the compressible regime compared to the incompressible instance.

a) *Tait parameter variation (m,B):* We conduct a Tait parameter sensitivity analysis to assess variation with the compressibility parameter set (m,B). First, we highlight the ability of the compressible algorithm to deal with a range of low Mach number ($0 < Ma < 0.2$), approaching the asymptotic limit $Ma \approx 0$. Figure 14 presents trends in solution profiles for different variables at the contraction channel centreline, based on variation in compressibility settings, adjusting Tait parameters accordingly. These trends reflect adjustment from the incompressible towards the mildly compressible setting ($Ma < 0.2$). In the compressible regime, only piecewise-constant density interpolation has been employed, as both constant and linear representations lead to practically identical results. Centreline solution profiles indicate that the compressibility setting has little affect on the velocity field before the contraction. As the flow becomes more compressible, some effects begin to appear beyond the contraction zone, once the liquid accelerates (17% faster for $(m,B)=(5,3000)$) above incompressible instance. At flow-entry, pressure and density are larger for compressible above incompressible flow (8% for pressure and 17% for density for $(m,B)=(5,3000)$). This highlights how much ‘compressibility’ impacts upon the flow kinematics.

Second, in Figure 15, we provide compressible flow history numerical convergence trends to steady-state for variation in (m,B) parameter set based upon increasing (Ma,ρ). Experience shows that this is the important paring to extract corresponding convergence behaviour in time. This covers $0.003 < Ma < 0.12$ and $1.0001 < \rho < 1.13$. All solutions are pursued to a limiting tolerance of 10^{-8} , though presentation in Figure 15 is restricted for comparison purposes, to the first 1000 time-steps at a common time-step value of $5 \cdot 10^{-2}$. We comment that where convergence trends are replicated, across (m,B) setting providing similar (Ma,ρ), say (m -variable, $B=10^4$) and ($m=1,B$ -variable), practically identical field solutions are obtained at steady-state.

At low Ma , $Ma < 0.005$: high-frequency/low-amplitude oscillations are a characteristic in the pressure norm $E^t(P)$ at early time (within the first 100 time-steps). The velocity norm $E^t(U)$ remains smooth. The rate of convergence is higher in pressure ($O(\Delta t^3)$) than in velocity ($O(\Delta t^{2.9})$) up to around 250 time-steps, after which time both norms converge at the same rate (that of velocity, with sustained gap between norms and monotonic linear trends).

At moderate Ma (applicable for liquids), $0.01 < Ma < 0.08$: there is elongation in pressure norm oscillations, decreasing in frequency with increasing Ma . Trends are characterised by lower frequency but larger amplitude pressure norm oscillations than for the low Ma -range. Velocity norm oscillations begin to appear at and above $Ma = 0.03$, spreading in time with increasing Ma . The pressure norm oscillations remain in phase with and some three-times larger than those in velocity, though clearly one drives the other. Equitable convergence rates throughout time now begin to arise in both norms. Averaged rates are linear and monotonic in pattern, being of order $E^t \approx O(\Delta t^{2.1})$. Oscillatory $E^t(P)$ patterns in $m=5$ sub-figures (e-g) are typical of convergence in a Lyapunov norm, as the theory would predict (see Van Kan (1986)).

For $Ma > 0.1$: oscillations in pressure and velocity norms disappear, so that convergence trends are smooth, with monotonic linear convergence-patterns of equitable order, $E^t \approx O(\Delta t^{1.3})$. The marked difference here is the unification of convergence norm values through time between the two variables of velocity and pressure. Clearly, the overall time to achieve the limiting convergence tolerance of 10^{-8} will imply an increase in the number of time-steps required. In the larger $Ma \approx 0.12$ instance, this leads to 1690 time-steps. This adjusts to 865 for $Ma \approx 0.04$ and 750 for $Ma \approx 0.005$.

We conclude that such trends in numerical convergence behaviour may be harnessed to gather the most preferable form for the instance in hand; speed in steady-state extraction or

matching both norms, $E^t(P)$ and $E^t(U)$. We note that it is the particular level of (Ma, ρ) that dictates the numerical convergence response. Nevertheless, we may be able to take advantage of superior convergence properties in adjusting (m, B) to arrive at a final steady-state for the target pairing. We attribute the linearization of the $E^t(P)$ norms with increasing Ma to the increased influence of the M_c -matrix in stage 2 (see Eq.(16)), an addition which vanishes at steady-state. When only steady-state is sought, convergence behaviour could be enhanced by choosing a large local time-step for stage 2. We note that by design, the present approach is lacking to describe highly-compressible flow ($Ma \gg O(1)$), as amongst other things, this would necessitate consideration of a kinetic equation (which is neglected here). Our experience is that numerical scaling on the pressure time-step at stage 2, ($\Delta t_p = \beta \Delta t$) may be a useful ploy that effectively switches the prevailing numerical value of the speed of sound (c) in the denominator of M_c , thus capturing the temporal convergence trend of an alternative physical (Ma, ρ) -pairing. To demonstrate this for $\Delta t = 0.05$, we have taken $(Ma = 0.12, \rho = 1.13, \beta = 1)$ and rescaled with $\beta = 10$ to mimic $(Ma = 0.03, \rho = 1.01, \beta = 10)$, for which we gather corresponding history norm convergence plots of Figures 15 (i) and (e). This may be repeated with $\beta = 10^3$ to mimic $(Ma = 0.003, \rho = 1.0001, \beta = 10^3)$ to recover Figure 15 (a) convergence pattern. There is a strong resemblance here to pseudo-compressible and artificial compressible implementations, employed for incompressible flows, in the sense of stage 2 conditioning on the lhs of the equation.

b) Tending towards the incompressible limit ($Ma \rightarrow 0$): Here, we address the effectiveness of the compressible implementation to deal with very low Mach number situations ($Ma \approx 0$), via adjustment of the Tait parameter pairing (m, B) , to mimic such a state. To this end, in Figure 16, the Tait parameters are elevated to high levels ($m = 10^2$ or 10^3 and $B = 10^5$), and one observes improvement in stability and convergence-rate of the

compressible versus the incompressible implementations. At this level of Tait parameters we observe high-frequency/low-amplitude pressure oscillations for incompressible convergence trends that are practically suppressed in the compressible instance. This is attributed to improvement in system condition number, via inclusion of the stage 2 mass-matrix and right-hand-side terms. Sample solution values for this particular case are tabulated in Table VI. The data highlight the match in sample centreline solution values, between incompressible and compressible (with $Ma \approx 0$) algorithmic implementations, in all variables and over different regions. Results demonstrate that, in the zero Mach number limiting regime, piecewise-constant density interpolation, with recovery of gradients during the second stage, is equitable to linear density interpolation. On the other hand, there is less than 0.5% overall difference between incompressible and compressible representations. Based on these findings, we have established that the compressible algorithmic implementations may be employed effectively to simulate weakly-compressible, as well as incompressible flow scenarios.

7. CONCLUSIONS

Based on a second order FE approximation with a pressure-correction method split into three distinguish fractional stages, two algorithmic representations have been introduced to simulate weakly-compressible highly-viscous polymeric liquid flow. The first uses a piecewise-constant density interpolation on the finite element, with nodal-recovery to compute the gradient of density. The second variant is based on a linear interpolation for the density (hence, piecewise-constant density gradient).

Consistency, accuracy and convergence have been assessed on a series of benchmark problems to highlight the performance of both interpolation variants. There is no apparent loss of accuracy incurred through these compressible interpolation variants, as compared to

their incompressible counterpart on these test problems. This is anticipated to reach a third-order for continuous problems. The convergence-rate to steady-state of both interpolation-forms is improved upon, as compared to that of the incompressible flow algorithm. This is attributed to the improvement in system condition number via the mass-matrix and right-hand-side contribution to the second-stage equation (for pressure). We have established temporal convergence patterns for compressible implementations conveying alternative ranges of (Ma, ρ) . Also, we have been able to point to scaling adjustment to improve convergence behaviour to steady-state solutions.

These compressible algorithmic variants have been shown capable of simulating flow with low to zero Mach number. Hence, a zero Mach number limit may be reached by adjusting Tait parameter pairings, where compressibility effects within the liquid flow may be controlled whilst approaching the incompressible limit. Under such circumstances, results match well with those for the compressible algorithm and those for the ‘purely’ incompressible algorithm. These findings allow the user to apply the compressible algorithm for both compressible and incompressible regimes.

The programming effort required to implement these compressible algorithms within an incompressible software framework has been manageable. The implementation is considerably easier for the piecewise-constant density interpolation (incompressible at the element-level, see Hawken *et al.*, 1990, for operation count analysis indicating linear time complexity on node (or element) counts per time-step, and linear space complexity overall). This necessitates a recovery technique for density gradients at stage two, with density scaling of all elemental matrices. In addition, low-order density interpolation with gradient recovery, has been found to perform equally as well as a linear density interpolation. On these grounds, the piecewise-constant interpolation is strongly

commended. Next, attention will be devoted to analysing viscoelastic counterpart flows, seeking to investigate the numerical and physical impact of this methodology there also.

ACKNOWLEDGMENTS

The financial support of EPSRC grant GR/R46885/01 is gratefully acknowledged. The second author welcomes the financial support of the Islamic Republic of Iran.

REFERENCES

- Baaijens, P. T. F. (1998) "Mixed finite element methods for viscoelastic flow analysis: a review", *Journal of Non-Newtonian Fluid Mechanics*, Vol 79, No 2-3, pp. 361-385.
- Baloch, A., Grant, P. W. and Webster, M. F. (2002) "Parallel computation of two-dimensional rotational flows of viscoelastic fluids in cylindrical vessels", *Engineering Computations*, Vol 19, No 7, pp. 820 - 853.
- Bijl, H. and Wesseling, P. (1998) "A unified method for computing incompressible and compressible flows in boundary-fitted coordinates", *Journal of Computational Physics*, Vol 141, No 2, pp. 153-173.
- Brujan, E. A. (1999) "A first-order model for bubble dynamics in a compressible viscoelastic liquid", *Journal of Non-Newtonian Fluid Mechanics*, Vol 84, No 1, pp. 83-103.
- Chorin, A. J. (1968) "Numerical solution of the Navier-Stokes equations", *Mathematics of Computation*, Vol 22, pp. 745-762.
- Ding, D., Townsend, P. and Webster, M. F. (1995) "On computation of two and three-dimensional unsteady thermal non-Newtonian flows", *International Journal of Numerical Methods in Heat and Fluid Flow*, Vol 5, No 6, pp. 495-510.
- Donea, J., Giuliani, S., Laval, H. and Quartapelle, L. (1982) "Finite element solution of the unsteady Navier-Stokes equations by fractional step method", *Computer Methods in Applied Mechanics and Engineering*, Vol 30, pp. 53-73.
- Field, J. E. (1999) "ELSI conference: invited lecture: Liquid impact: theory, experiment, applications", *Wear*, Vol 233-235, pp. 1-12.
- Georgiou, G. C. (2003) "The time-dependent, compressible Poiseuille and extrudate-swell flows of a Carreau fluid with slip at the wall", *Journal of Non-Newtonian Fluid Mechanics*, Vol 109, No 2-3, pp. 93-114.

- Ghia, U., Ghia, K. N. and Shin, C. (1982) "High-Re solutions for incompressible flow using the Navier-Stokes equations and a multigrid method", *Journal of Computational Physics*, Vol 48, pp. 387-411.
- Guénette, R. and Fortin, M. (1995) "A new mixed finite element method for computing viscoelastic flows", *Journal of Non-Newtonian Fluid Mechanics*, Vol 60, No 1, pp. 27-52.
- Guillard, H. and Viozat, C. (1999) "On the behaviour of upwind schemes in the low Mach number limit", *Computers & Fluids*, Vol 28, No 1, pp. 63-86.
- Han, K.-H. and Im, Y.-T. (1997) "Compressible flow analysis of filling and post-filling in injection molding with phase-change effect", *Composite Structures*, Vol 38, No 1-4, pp. 179-190.
- Harlow, F. H. and Amsden, A. (1968) "Numerical calculation of almost incompressible flow", *Journal of Computational Physics*, Vol 3, pp. 80-93.
- Hawken, D. M., Tamaddon-Jahromi, H. R., Townsend, P. and Webster, M. F. (1990) "A Taylor-Galerkin based algorithm for viscous incompressible flow", *International Journal for Numerical Methods in Fluids*, Vol 10, pp. 327-351.
- Huang, Y. K. and Chow, C. Y. (1974) "The generalized compressibility equation of Tait for dense matter", *Journal of Physics D: Applied Physics*, Vol 7, pp. 2021-2023.
- Hughes, T. J. R., Franca, L. P. and Hulbert, G. M. (1989) "A new finite element formulation for computational fluid dynamics: VIII. The Galerkin Least-Squares method for advective diffusive equations", *Computer Methods in Applied Mechanics and Engineering*, Vol 73, p 173–189.
- Jackson, M. J. and Field, J. E. (1999) "Liquid impact erosion of single-crystal magnesium oxide", *Wear*, Vol 233-235, pp. 39-50.

- Jenny, P. and Muller, B. (1999) "Convergence acceleration for computing steady-state compressible flow at low Mach numbers", *Computers & Fluids*, Vol 28, No 8, pp. 951-972.
- Karimian, S. M. H. and Schneider, G. E. (1995) "Pressure-based control-volume finite-element method for flow at all speeds", *AIAA journal*, Vol 33, No 9, pp. 1611-1618.
- Karki, K. and Patankar, S. V. (1989) "Pressure based calculation procedure for viscous flows at all speeds in arbitrary configurations", *AIAA journal*, Vol 27, No 9, pp. 1167-1174.
- Kelmanson, M. A. and Maunder, S. B. (1999) "Modelling high-velocity impact phenomena using unstructured dynamically-adaptive Eulerian meshes", *Journal of the Mechanics and Physics of Solids*, Vol 47, No 4, pp. 731-762.
- Keshtiban , I. J., Belblidia, F. and Webster, M. F.,(2003) "Review of compressible flow solvers for low Mach number flows: density-based approach," Computer Science Technical Report., University of Wales Swansea, UK.
- Lien, F. S. and Leschziner, M. A. (1993) "A pressure velocity solution strategy for compressible flow and its application to shock boundary layer interaction using second-moment turbulence closure", *Journal of Fluid Engineering*, Vol 115, No DEC, pp. 717-725.
- Löhner, R., Morgan, K. and Zienkiewicz, O. C. (1984) "The solution of non-linear hyperbolic equation systems by the finite element method", *International Journal for Numerical Methods in Fluids*, Vol 4, pp. 1043-1063.
- Mary, I., Sagaut, P. and Deville, M. (2000) "An algorithm for low Mach number unsteady flows", *Computers & Fluids*, Vol 29, No 2, pp. 119-147.

- Matallah, H., Townsend, P. and Webster, M. F. (1998) "Recovery and stress-splitting schemes for viscoelastic flows", *Journal of Non-Newtonian Fluid Mechanics*, Vol 75, No 2-3, pp. 139-166.
- Moukalled, F. and Darwish, M. (2001) "A high-resolution pressure-based algorithm for fluid Flow at all speeds", *Journal of Computational Physics*, Vol 168, No 1, pp. 101-133.
- Munz, C.-D., Roller, S., Klein, R. and Geratz, K. J. (2003) "The extension of incompressible flow solvers to the weakly compressible regime", *Computers & Fluids*, Vol 32, No 2, pp. 173-196.
- Ngamaramvaranggul, V. and Webster, M. F. (2000a) "Computation of free surface flows with a Taylor-Galerkin/pressure-correction algorithm", *International Journal for Numerical Methods in Fluids*, Vol 33, No 7, pp. 993-1026.
- Ngamaramvaranggul, V. and Webster, M. F. (2000b) "Simulation of coating flows with slip effects", *International Journal for Numerical Methods in Fluids*, Vol 33, No 7, pp. 961-992.
- Patankar, S. V. (1980) *Numerical heat transfer and fluid flow*, McGraw-Hill, New York.
- Peyret, R. and Taylor, T. D. (1983) *Computational Methods for Fluid Flow*, Springer-Verlag, New York.
- Ranganathan, M., Mackley, M. R. and Spitteler, P. H. J. (1999) "The application of the multipass Rheometer to time dependent capillary flow measurements of a Polyethylene melt", *Journal of Rheology*, Vol 43, No 2, pp. 443-451.
- Roller, S. and Munz, C. D. (2000) "A low Mach number scheme based on multi-scale asymptotics", *Computing and Visualization in Science*, Vol 3, No 1/2, pp. 85-91.

- Saramito, P. and Piau, J. M. (1994) "Flow characteristics of viscoelastic fluids in an abrupt contraction by using numerical modeling", *Journal of Non-Newtonian Fluid Mechanics*, Vol 52, No 2, p 263.
- Tait, P. G. (1888) "HSMO", *London*, Vol 2, No 4.
- Temam, R. (1969) "Sur l'approximation de la solution de Navier-Stokes par la méthode des pas fractionnaires", *Archiv. Ration. Mech. Anal.*, Vol 32, pp. 377-385.
- Turkel, E., Radespiel, R. and Kroll, N. (1997) "Assessment of preconditioning methods for multidimensional aerodynamics", *Computers & Fluids*, Vol 26, No 6, pp. 613-634.
- Van Kan, J. (1986) "A second-order accurate pressure-correction scheme for viscous incompressible flow", *SIAM Journal of Scientific and Statistical Computing*, Vol 7, pp. 870-891.
- Walters, K. and Webster, M. F. (2003) "The distinctive CFD challenges of computational rheology", *International Journal for Numerical Methods in Fluids*, Vol In press.
- Wapperom, P. and Webster, M. F. (1998) "A second-order hybrid finite-element/volume method for viscoelastic flows", *Journal of Non-Newtonian Fluid Mechanics*, Vol 79, No 2-3, pp. 405-431.
- Webster, M. F. and Townsend, P. (1990) In *Numerical Methods in Engineering: Theory and Applications - NUMETA*, Vol. 90 (Eds, Pande, G. N. and Middleton, J.) Elsevier Applied Science, London & New York.
- Wong, J. S., Darmofal, D. L. and Peraire, J. (2001) "The solution of the compressible Euler equations at low Mach numbers using a stabilized finite element algorithm", *Computer Methods in Applied Mechanics and Engineering*, Vol 190, No 43-44, pp. 5719-5737.

Wu, Y.-S. and Pruess, K. (2000) "Integral solutions for transient fluid flow through a porous medium with pressure-dependent permeability", *International Journal of Rock Mechanics and Mining Sciences*, Vol 37, No 1-2, pp. 51-61.

Zienkiewicz, O. C., Morgan, K., Sataya Sal, B. V. K., Codina, R. and Vasquez, M. (1995) "A general algorithm for compressible and incompressible flow - Part II . Test on the explicit form", *International Journal for Numerical Methods in Fluids*, Vol 20, pp. 887-913.

List of figures

- Figure 1.** Pressure (top) and streamlines (bottom) contours for cavity: Incompressible, case (b), $Re=100$ (left) and $Re=400$ (right)
- Figure 2.** U, V on vertical or horizontal cavity centrelines, incompressible, case (b), $Re=100$ and $Re=400$
- Figure 3.** Mach number contours for cavity: Piecewise-constant density interpolation, case (b), $Re=100$, $(m, B)=(2, 300)$
- Figure 4.** Infinity error norm $\|E_h\|_\infty$ on velocity for different algorithms for cavity, a) case (a), $Re=100$, b) case (b), $Re=100$, $(m, B)=(2, 300)$
- Figure 5.** Temporal convergence history trends for velocity, $E^t(U)$ (left) and pressure, $E^t(P)$ (right): Cavity problem based on $Re=100$ and $\Delta t=0.01$, case (b), $(m, B)=(2, 300)$
- Figure 6.** Channel flow, a) schema (showing (X, Y) locations, where solution sampled), b) U_x -Velocity contours, left: incompressible, right: linear $(m, B)=(2, 100)$, top: mesh $10*10$, middle: $20*20$, bottom: $40*40$
- Figure 7.** $Ma*10^2$ contours for channel, left: piecewise-constant, right: linear, top: mesh $10*10$, middle: $20*20$, bottom: $40*40$, $(m, B)=(2, 100)$
- Figure 8.** Contraction flow. a) schema, b-d) Mesh refinement around the contraction, M1-M3, d) Sample point locations on mesh M2 for axisymmetric and planar cases. (mesh characteristics in Table III)
- Figure 9.** Temporal convergence history trends for planar contraction flow, various algorithms: for pressure $E^t(P)$ (left) and velocity $E^t(U)$ (right); $(m, B)=(5, 3000)$, mesh refinement M1-M3

- Figure 10.** Pressure (right) and streamlines fields (left) for planar contraction flow problem, piecewise-constant density interpolation scheme, $(m,B)=(5,3000)$, mesh refinement M1-M3 (values in Table IV)
- Figure 11.** Density and Mach number for planar contraction flow, $(m,B)=(2,300)$; a) Density (linear interpolation), Mach number under b) piecewise density interpolation c) linear density interpolation (values in Table Va)
- Figure 12.** Solution profiles at channel centreline (planar case), piecewise-constant and linear density interpolation, $(m,B)=(2,300)$. Top left: velocity, top right: pressure, bottom left: density, bottom right: Mach number
- Figure 13.** Density and Mach number for circular contraction flow, $(m,B)=(5,3000)$; a) Density (linear interpolation), Mach number under b) piecewise density interpolation c) linear density interpolation (values in Table Vb)
- Figure 14.** Variation in compressibility settings, mildly compressible towards incompressible, trends in solution profiles on channel centreline (circular case), piecewise-constant density interpolation. top left: U_z -velocity, top right: pressure, bottom left: density, bottom right: Mach number
- Figure 15.** Effect of Tait parameter (m,B) variation on convergence history of pressure $E^t(P)$ and velocity $E^t(U)$, piecewise-constant density interpolation, increasing compressibility effect, circular contraction flow
- Figure 16.** Convergence history trends for (left) velocity $E^t(U)$ and (right) pressure $E^t(P)$, circular contraction flow, incompressible versus piecewise-constant density interpolation tending to the incompressible limit

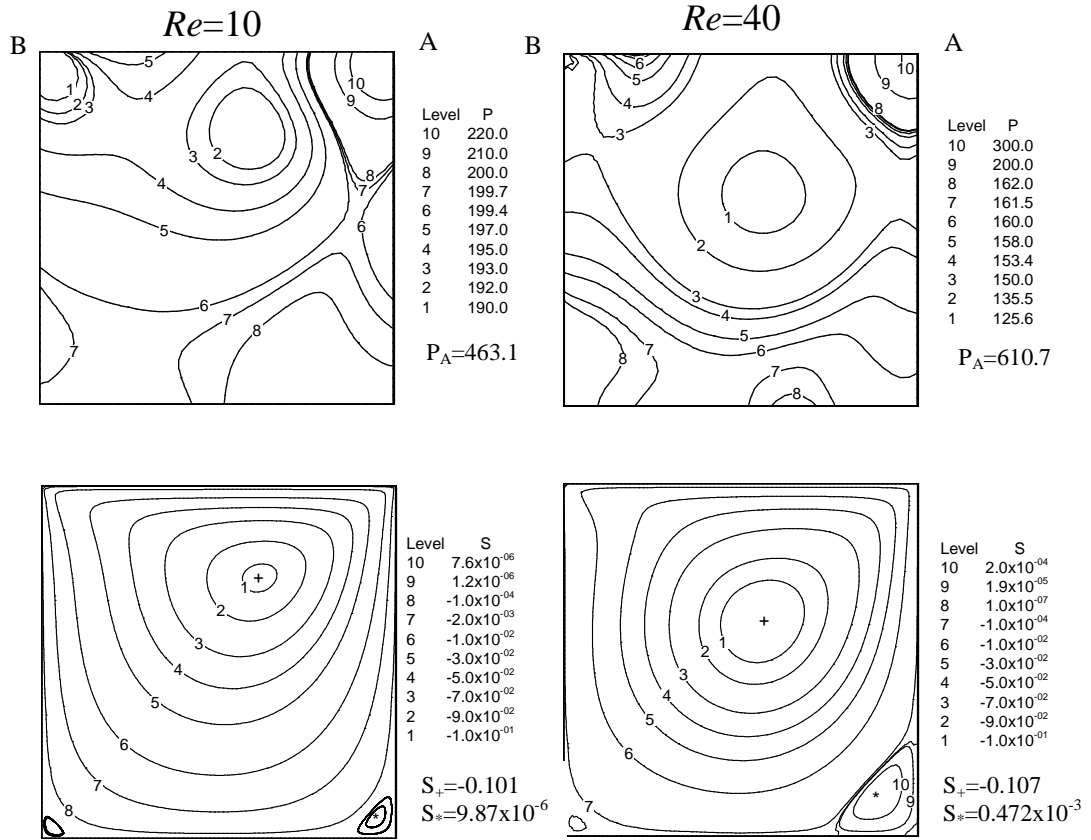


Figure 1. Pressure (top) and streamlines (bottom) contours for cavity:
Incompressible, case (b), $Re=100$ (left) and $Re=400$ (right)

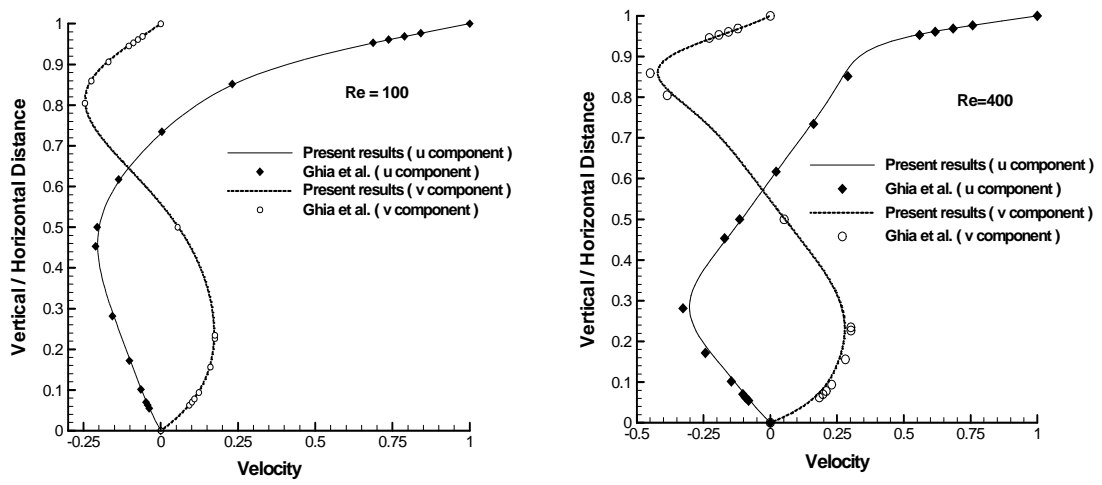


Figure 2. (U,V) on vertical or horizontal cavity centrelines, incompressible, case (b), $Re = 100$ and $Re = 400$

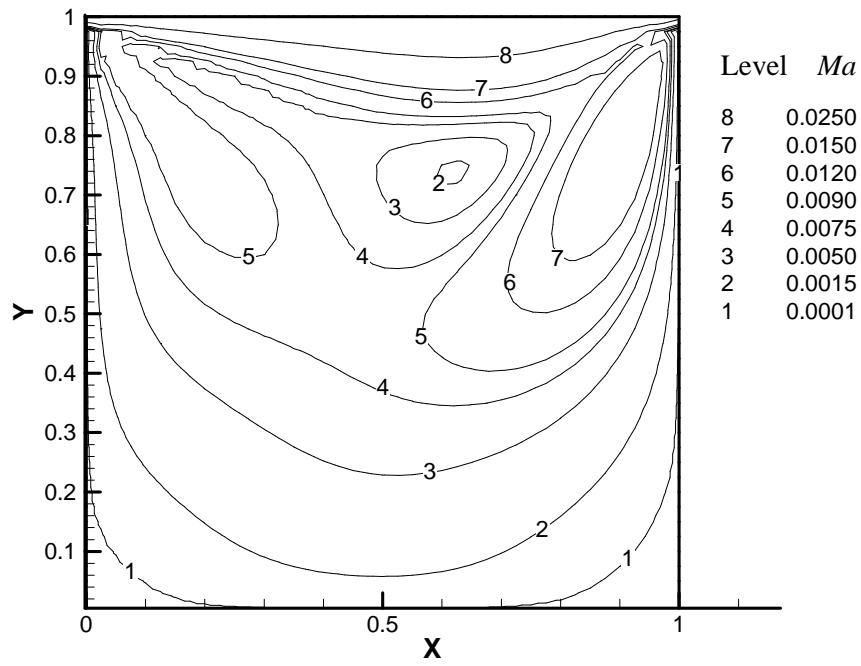


Figure 3. Mach number contours for cavity: Piecewise-constant density interpolation, case (b), $Re=100$, $(m,B)=(2,300)$

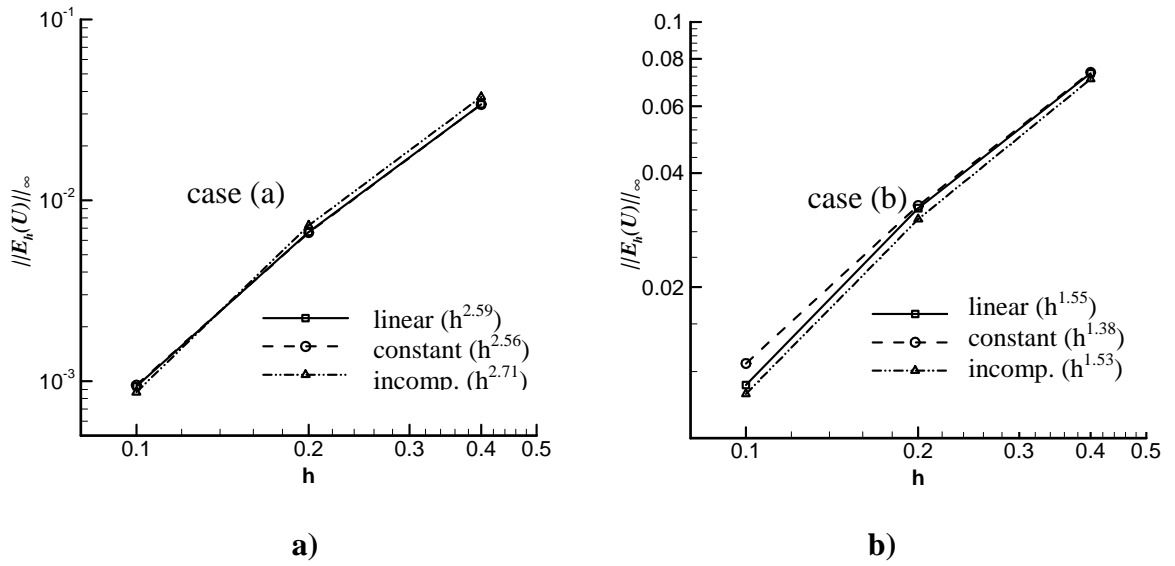


Figure 4. Infinity error norm $\|E_h\|_\infty$ on velocity for different algorithms for cavity, a) case (a), $Re=100$, b) case (b), $Re=100$, $(m,B)=(2,300)$

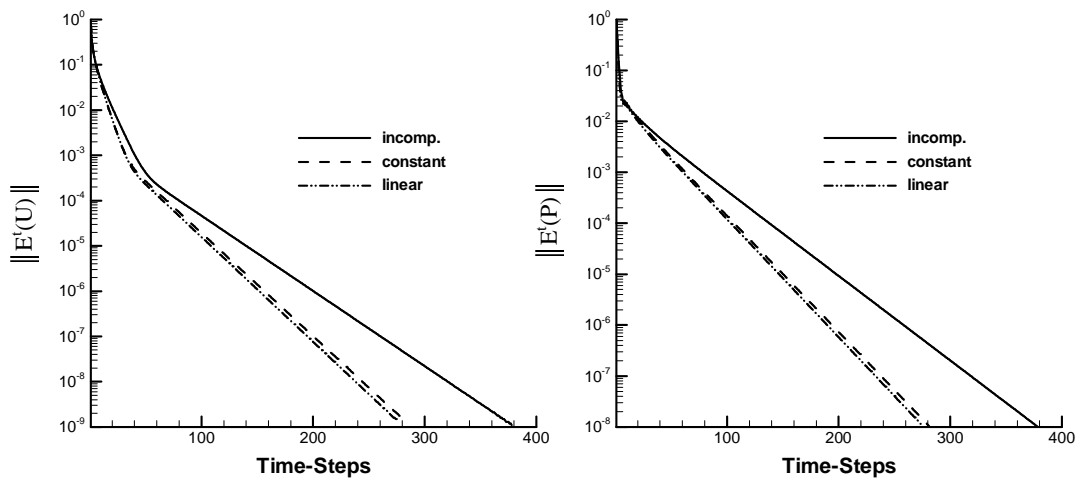
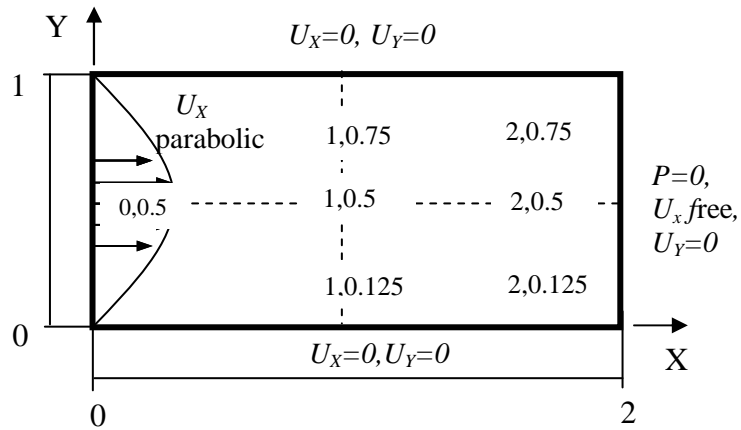
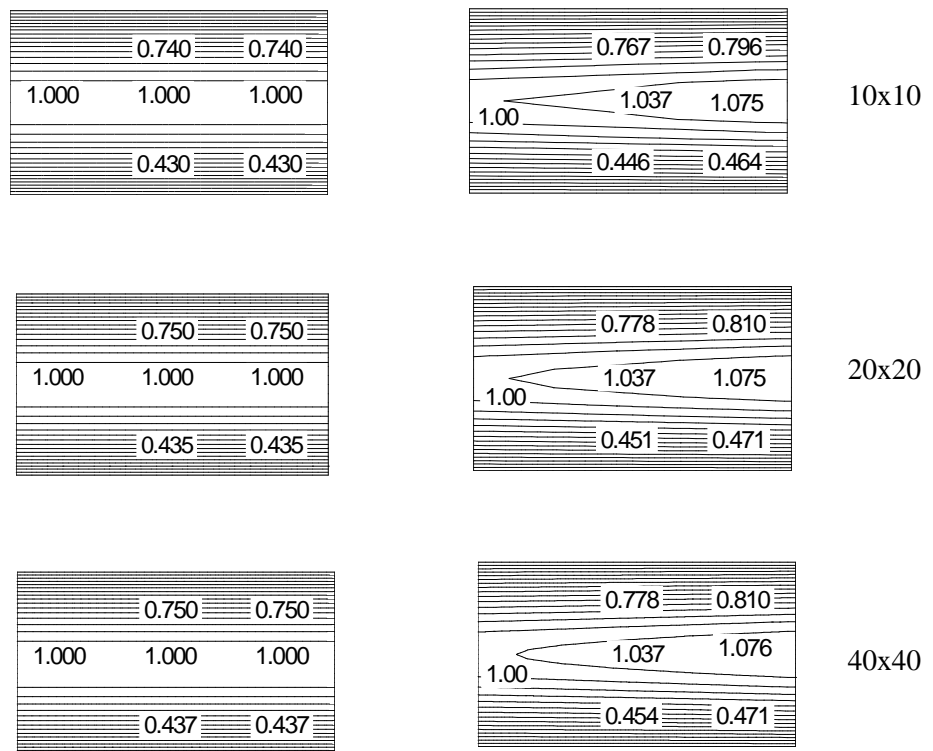


Figure 5. Temporal convergence history trends for velocity, $E^t(U)$ (left) and pressure, $E^t(P)$ (right): Cavity problem based on $Re=100$ and $\Delta t=0.01$, case (b), $(m,B)=(2,300)$



a)



Incompressible

Linear

b)

Figure 6. Channel flow

a) schema (showing (X,Y) locations, where solution sampled), b) U_x -Velocity contours, left: incompressible, right: linear (m, B)=(2,100), top: mesh 10*10, middle: 20*20, bottom: 40*40

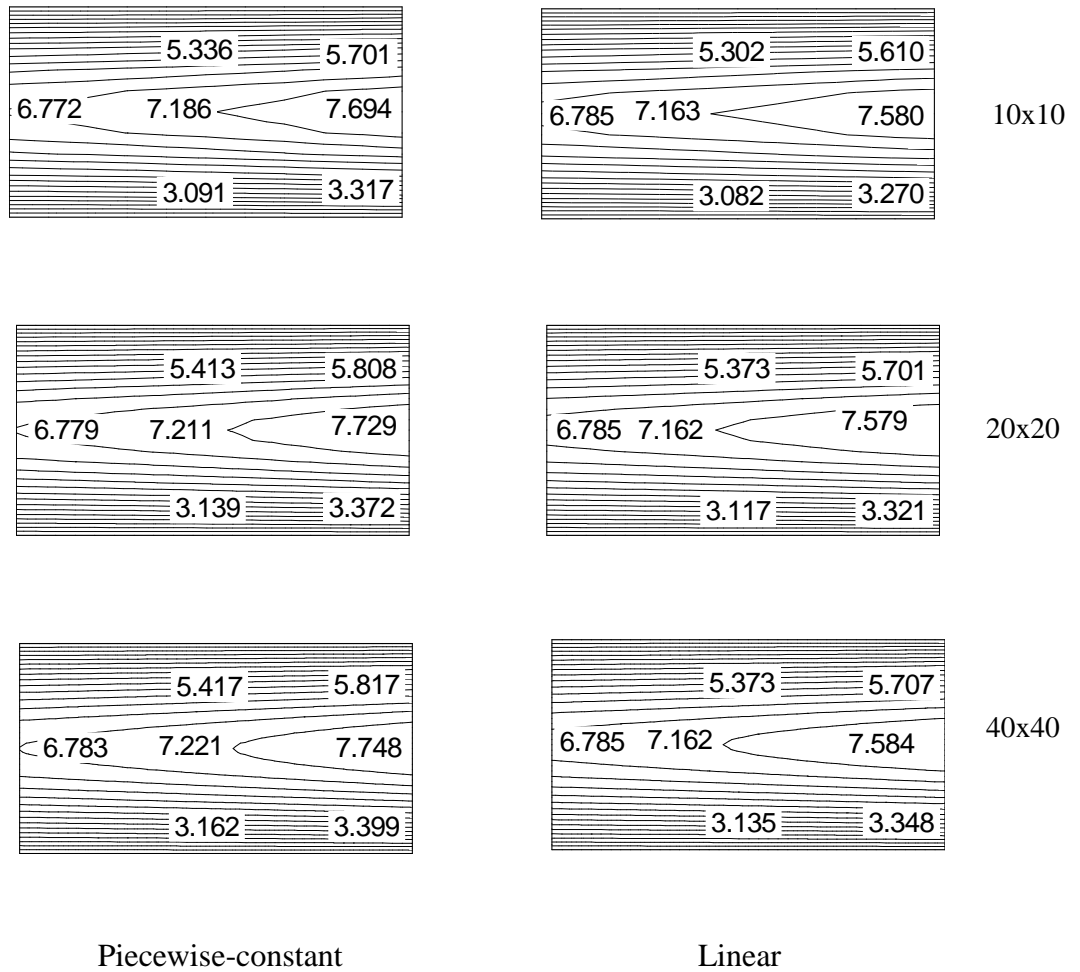


Figure 7. $Ma \cdot 10^2$ contours for channel, left: piecewise-constant, right: linear, top: mesh 10×10 , middle: 20×20 , bottom: 40×40 , $(m, B) = (2, 100)$

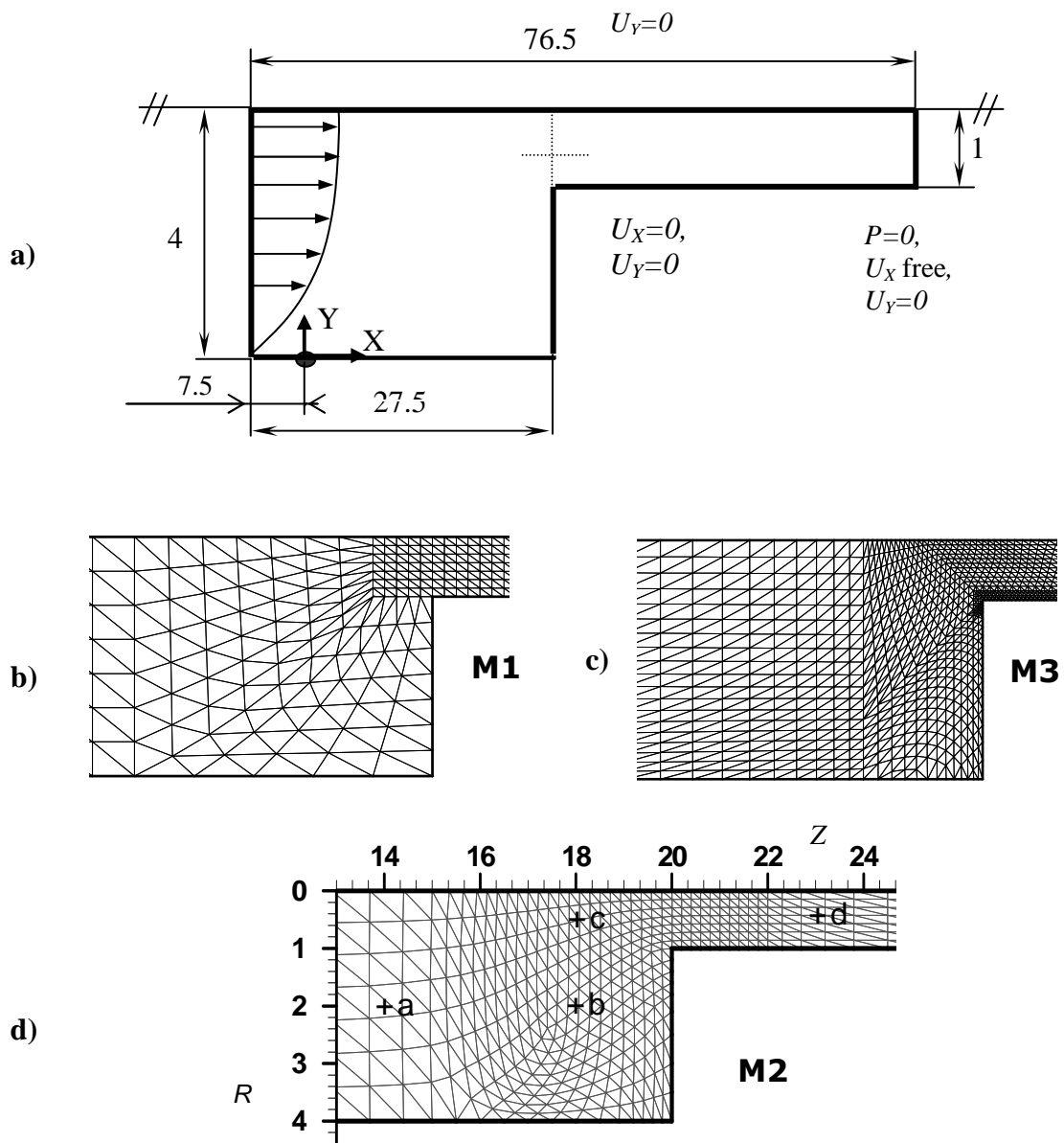


Figure 8. Contraction flow.

a) schema, b-d) Mesh refinement around the contraction, M1-M3),
 d) Sample point locations on mesh M2 for axisymmetric and planar cases. (mesh characteristics in Table III)

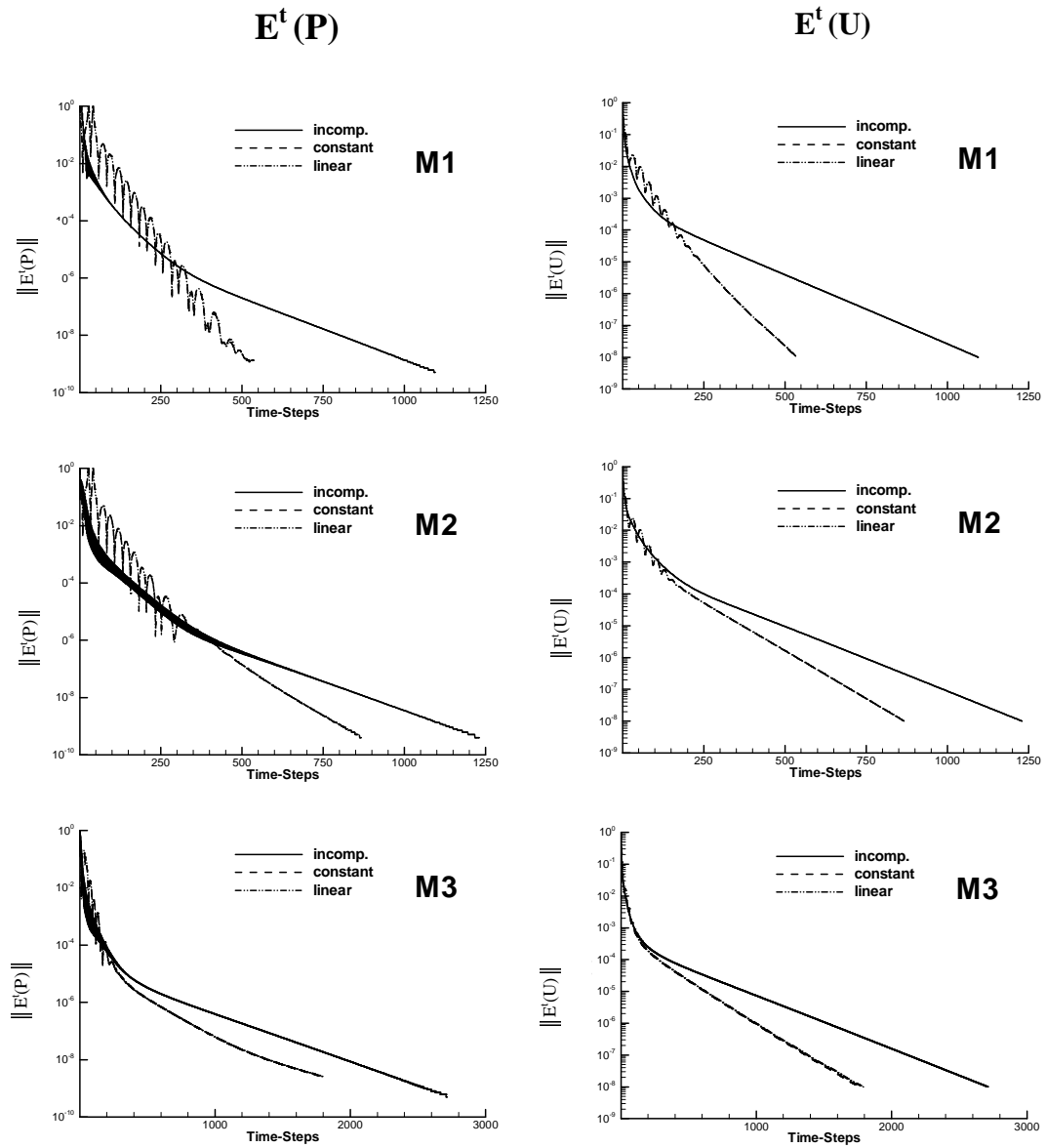


Figure 9. Temporal convergence history trends for planar contraction flow, various algorithms: for pressure $E^t(P)$ (left) and velocity $E^t(U)$ (right); $(m,B)=(5,3000)$, mesh refinement ~~M1~~-M3

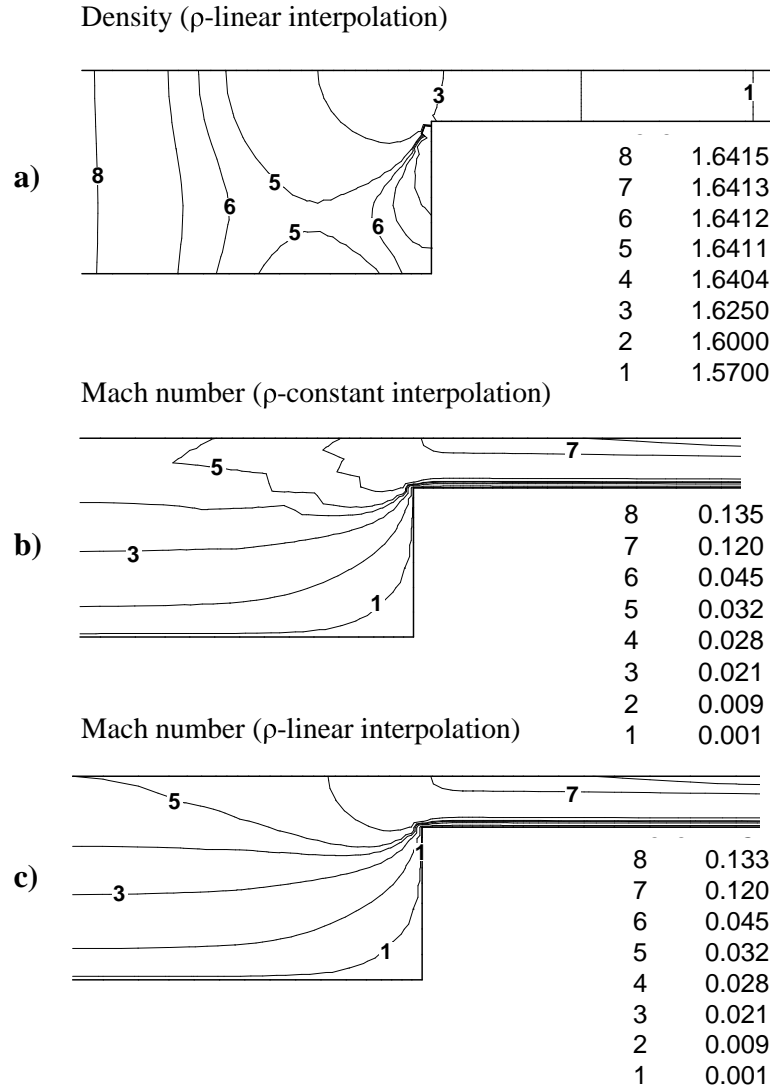


Figure 10. Pressure (right) and streamlines fields (left) for planar contraction flow, piecewise-constant density interpolation scheme, $(m, B) = (5, 3000)$, mesh refinement M1-M3 (values in Table IV)

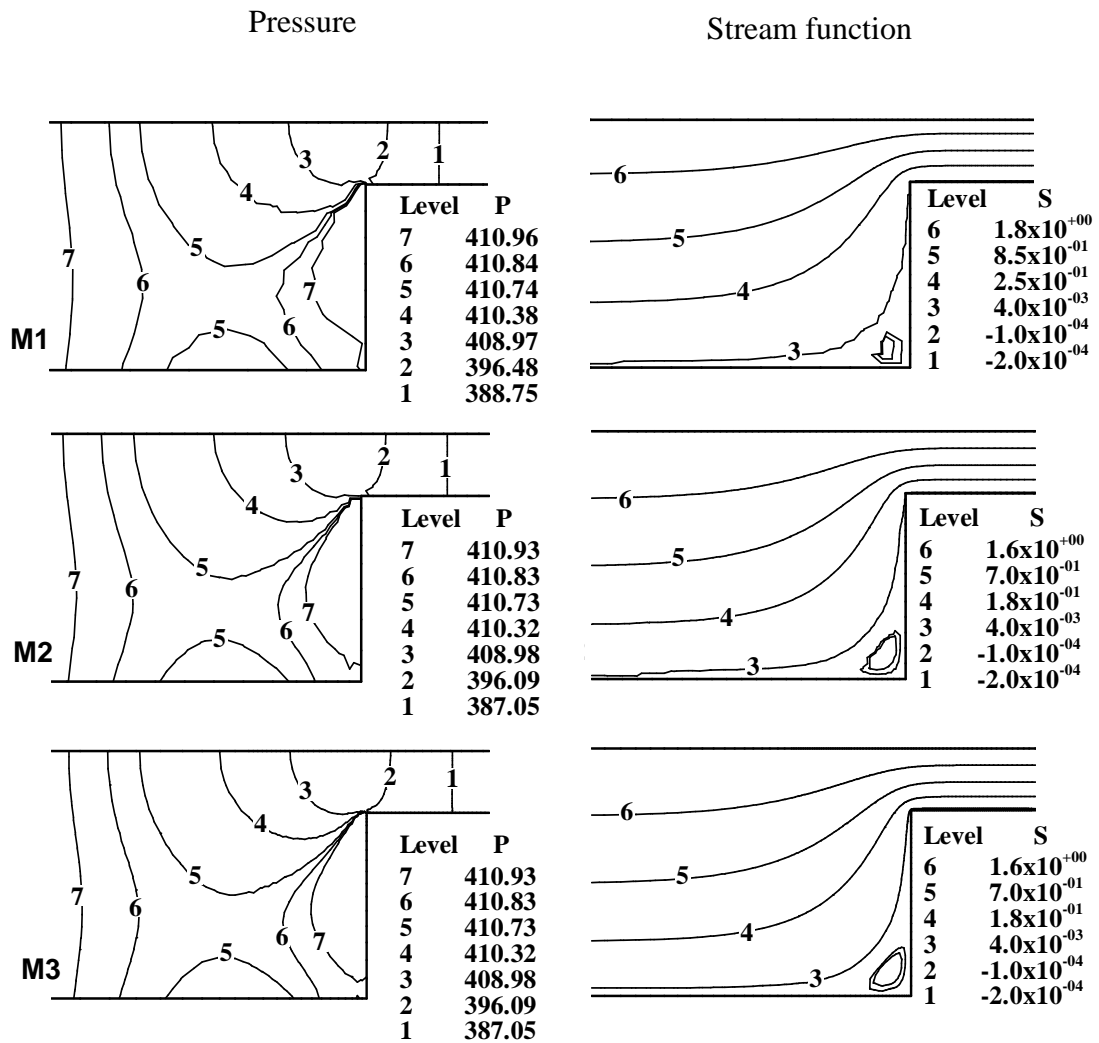


Figure 11. Density and Mach number for planar contraction flow, $(m,B)=(2,300)$; a) Density (linear interpolation), Mach number under b) piecewise density interpolation c) linear density interpolation (values in Table Va)

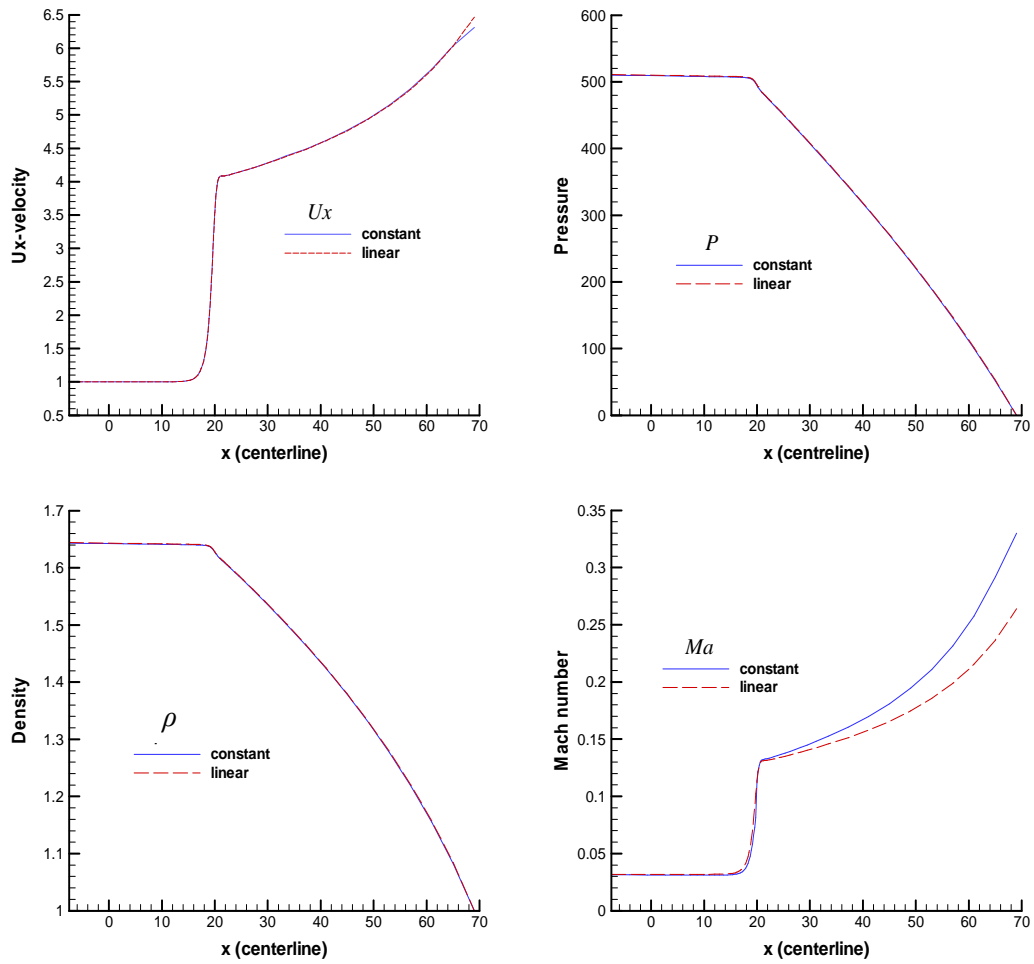


Figure 12. Solution profiles at channel centreline (planar case), piecewise-constant and linear density interpolation, $(m,B)=(2,300)$. Top left: velocity, top right: pressure, bottom left: density, bottom right: Mach number

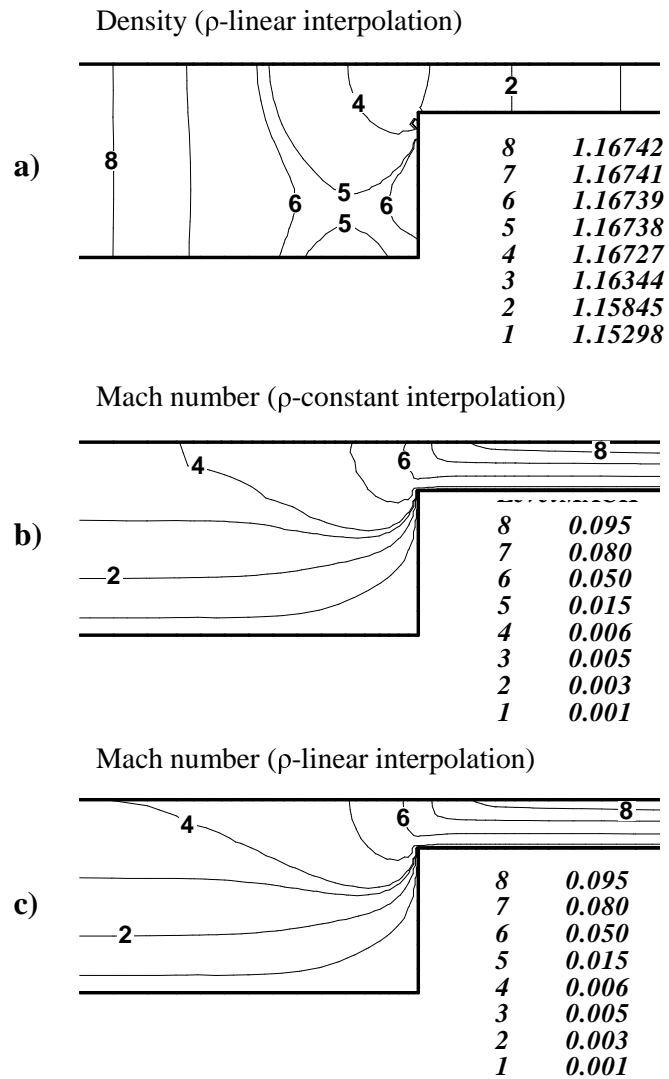


Figure 13. Density and Mach number for circular contraction flow, $(m,B)=(5,3000)$; a) Density (linear interpolation), Mach number under b) piecewise density interpolation c) linear density interpolation (values in Table Vb)

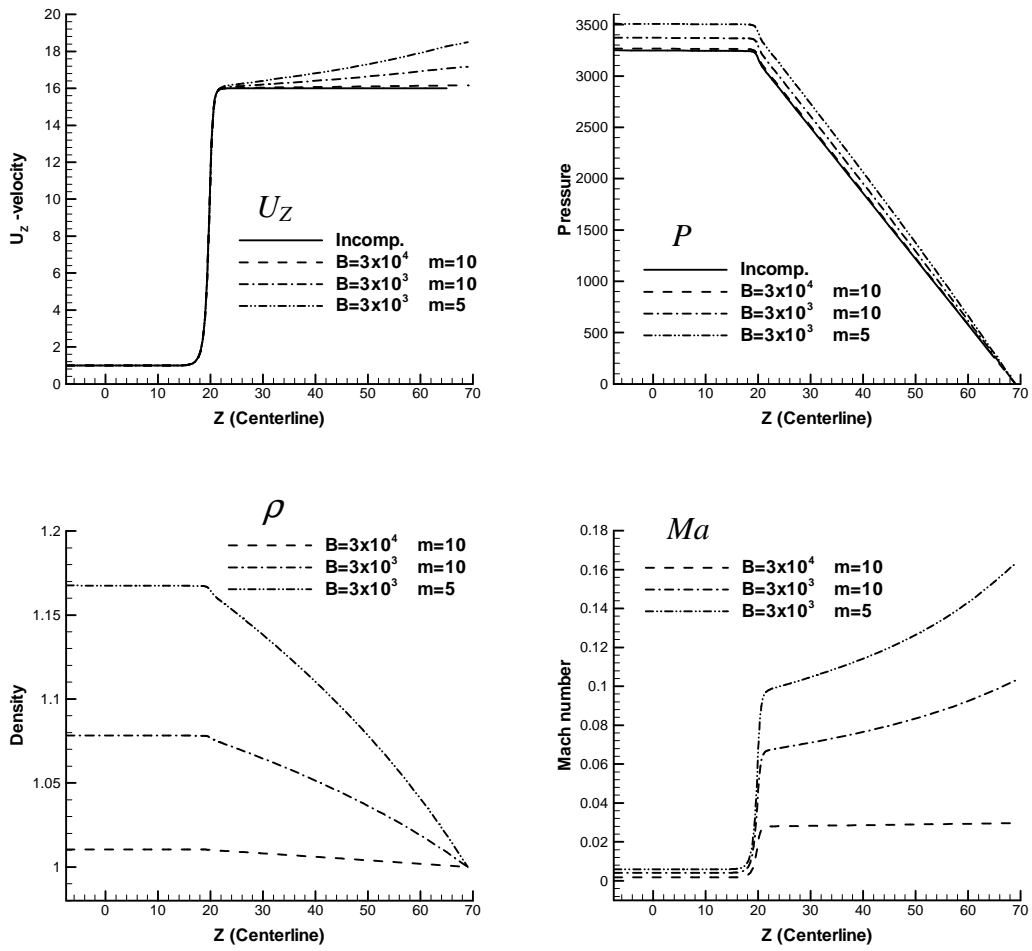


Figure 14. Variation in compressibility settings, mildly compressible towards incompressible, trends in solution profiles on channel centreline (circular case), piecewise-constant density interpolation. top left: U_Z -velocity, top right: pressure, bottom left: density, bottom right: Mach number

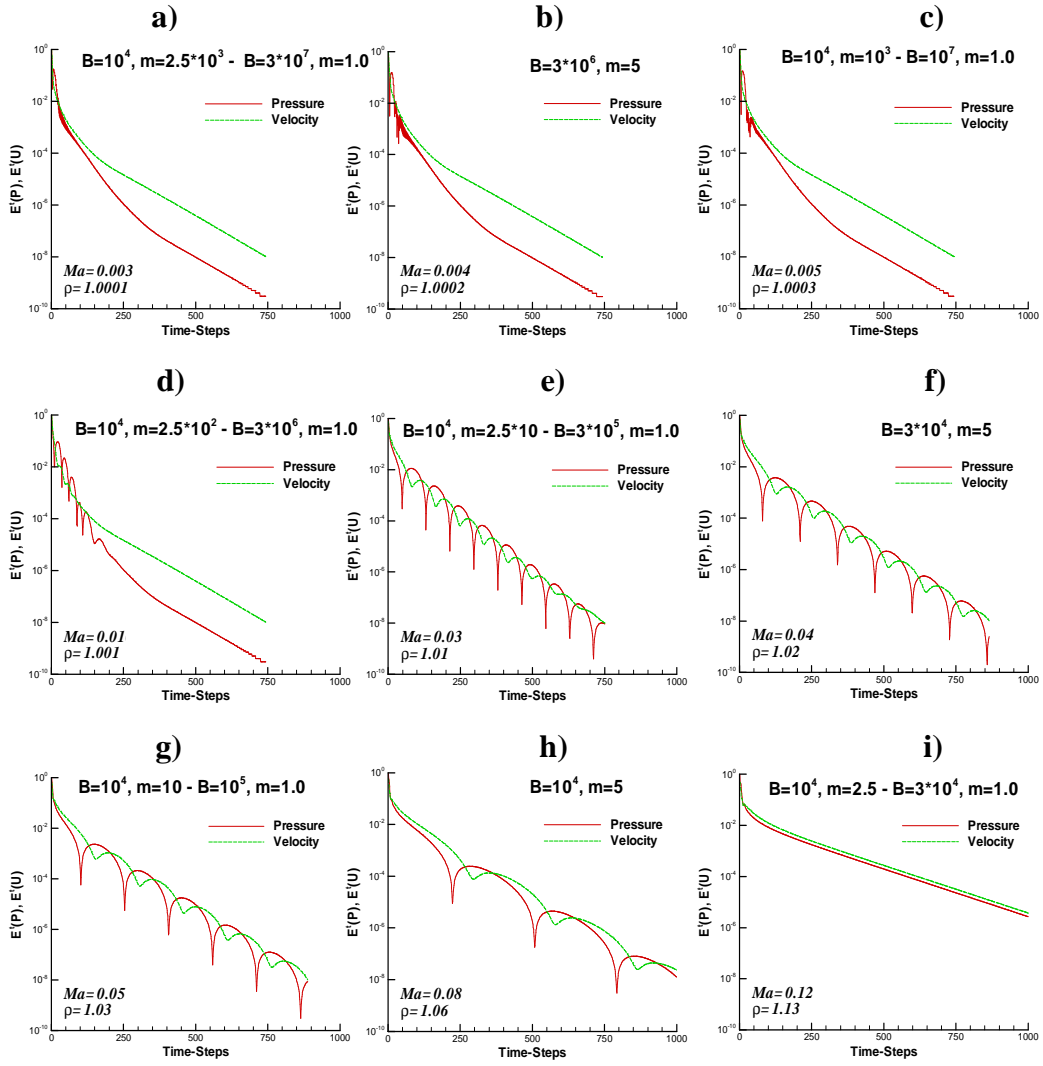


Figure 15. Effect of Tait parameter (m, B) variation on convergence history of pressure $E^t(P)$ and velocity $E^t(U)$, piecewise-constant density interpolation, increasing compressibility effect, circular contraction flow

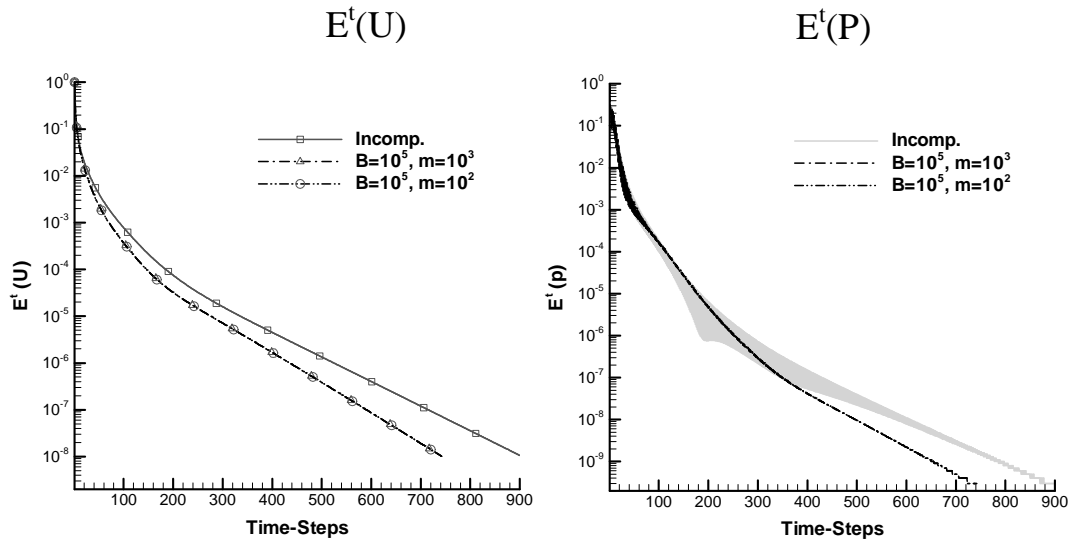


Figure 16. Convergence history trends for (left) velocity $E^t(U)$ and (right) pressure $E^t(p)$, circular contraction flow problem, incompressible versus piecewise-constant density interpolation tending to the incompressible limit

List of tables

- Table I.** Error on mass balance for channel flow under different regimes and meshes, $(m,B)=(2,100)$
- Table II.** Pressure and density values for channel flow under three regimes, centreline various X-locations with mesh-size variation, $(m,B)=(2,100)$
- Table III.** Mesh characteristic parameters for contraction flow
- Table IV.** Sample pressure and velocity components values at contraction and vortex information, various meshes and different algorithms, planar contraction flow, $(m,B)=(5,3000)$
- Table V.** Solution values at sampled spatial locations of contraction flow, various algorithms, a) planar case, $(m,B)=(2,300)$, b) circular case, $(m,B)=(5,3000)$
- Table VI.** Sampled centreline solution values, various algorithms, towards zero Mach number (circular case)

Table I. Error on mass balance for channel flow under different regimes and meshes,
 $(m,B)=(2,100)$

Mesh	Incompressible			Piecewise-constant			Linear		
	Inlet	Outlet	<i>%Error</i>	Inlet	Outlet	<i>%Error</i>	Inlet	Outlet	<i>%Error</i>
10*10	0.6667	0.6650	<i>0.250</i>	0.7148	0.7088	<i>0.832</i>	0.7148	0.7130	<i>0.259</i>
20*20	0.6667	0.6625	<i>0.063</i>	0.7160	0.7131	<i>0.407</i>	0.7162	0.7152	<i>0.137</i>
40*40	0.6667	0.6666	<i>0.016</i>	0.7164	0.7149	<i>0.209</i>	0.7165	0.7160	<i>0.076</i>

Table II. Pressure and density values for channel flow under three regimes, centreline various X-locations with mesh-size variation, $(m,B)=(2,100)$

		X-positions	Mesh 10*10	Mesh 20*20	Mesh 40*40
Pressure	Incompressible	0.0	16.000	16.000	16.000
		0.5	12.000	12.000	12.000
		1.0	8.000	8.000	8.000
		1.5	4.000	4.000	4.000
	Piecewise-constant	0.0	16.623	16.656	16.665
		0.5	12.613	12.639	12.647
		1.0	8.506	8.525	8.531
		1.5	4.320	4.331	4.335
	Linear	0.0	16.795	16.812	16.822
		0.5	12.754	12.763	12.774
		1.0	8.627	8.644	8.654
		1.5	4.424	4.444	4.454
Density	Piecewise-constant	0.0	1.075	1.075	1.075
		0.5	1.056	1.056	1.057
		1.0	1.036	1.037	1.037
		1.5	1.016	1.016	1.016
		2.0	0.995	0.995	0.995
	Linear	0.0	1.075	1.075	1.076
		0.5	1.057	1.057	1.057
		1.0	1.037	1.037	1.037
		1.5	1.017	1.017	1.017
		2.0	0.996	0.996	0.996

Table III. Mesh characteristic parameters for contraction flow

	M1	M2	M3
Elements	980	1140	2987
Nodes	2105	2427	6220
Vertex Nodes	563	644	1617
d.o.f.	8983	9708	14057
R_{\min}	0.024	0.023	0.011
Corner mesh density	28	63	201

Table IV. Sample pressure and velocity components values at contraction and vortex information, various meshes and different algorithms, planar contraction flow, $(m,B)=(5,3000)$

		M1	M2	M3
Pressure	Incompressible	393.6	393.5	393.5
	ρ -Constant	400.4	400.4	400.3
	ρ -Linear	400.4	400.4	400.4
U_x	Incompressible	2.957	2.956	2.969
	ρ -Constant	2.953	2.954	2.971
	ρ -Linear	2.953	2.954	2.971
U_y	Incompressible	0.520	0.516	0.518
	ρ -Constant	0.533	0.526	0.523
	ρ -Linear	0.533	0.526	0.523
S_{\min} at vortex (-10^{-3})	ρ -Constant	0.324	0.449	0.414

Table V. Solution values at sampled spatial locations of contraction flow, various algorithms, a) planar case, $(m,B)=(2,300)$, b) circular case, $(m,B)=(5,3000)$

a) Planar

Sample locations	U_x -velocity			Pressure			Density		Mach number	
	incomp.	compressible		incomp.	compressible		compressible		compressible	
		ρ -constant	ρ -linear		ρ -constant	ρ -linear	ρ -constant	ρ -linear	ρ -constant	ρ -linear
a	0.743	0.744	0.745	404.1	507.5	508.3	1.6406	1.6414	0.0234	0.0237
b	0.596	0.621	0.621	403.7	507.1	507.9	1.6402	1.6410	0.0212	0.0212
c	1.323	1.281	1.281	403.1	506.4	507.2	1.6394	1.6403	0.0377	0.0412
d	2.979	3.063	3.063	367.9	466.9	467.6	1.5988	1.5996	0.0998	0.0989

b) Axisymmetric

Sample locations	U_z -velocity			Pressure			Density		Mach number	
	incomp.	compressible		incomp.	compressible		compressible		compressible	
		ρ -constant	ρ -linear		ρ -constant	ρ -linear	ρ -constant	ρ -linear	ρ -constant	ρ -linear
a	0.746	0.746	0.746	3244.5	3503.4	3505.1	1.1674	1.1674	0.0044	0.0045
b	0.734	0.737	0.737	3243.5	3502.4	3504.0	1.1673	1.1674	0.0047	0.0047
c	1.614	1.580	1.580	3242.6	3501.5	3503.1	1.1673	1.1674	0.0092	0.0095
d	11.918	12.036	12.035	2944.0	3188.3	3189.9	1.1558	1.1559	0.0738	0.0735

Table VI. Sampled centreline solution values, various algorithms, towards zero Mach number (circular case)

Variable	Z-position	Incompressible	Compressible			
			$m=10^3, B=10^5$		$m=10^2, B=10^5$	
			ρ -Constant	ρ -Linear	ρ -Constant	ρ -Linear
Uz	Contra.	11.4690	11.4149	11.4149	11.4145	11.4145
	52.0	15.9999	16.0002	16.0002	16.0026	16.0026
	Exit	15.9999	16.0004	16.0004	16.0048	16.0049
Pressure	Entry	3249.87	3249.47	3249.47	3249.99	3249.99
	Contra.	3170.96	3171.26	3171.26	3171.77	3171.77
	52.0	1535.99	1536.03	1536.03	1536.38	1536.38
Density	Entry	1.00000	1.00003	1.00003	1.00032	1.00032
	Contra.	1.00000	1.00003	1.00003	1.00031	1.00031
	52.0	1.00000	1.00005	1.00005	1.00015	1.00015
Mach	Entry	0.0000	9.84e-5	9.84e-5	0.0003	0.0003
	Contra.	0.0000	0.0011	0.0011	0.0036	0.0036
	52.0	0.0000	0.0016	0.0016	0.0052	0.0052
	Exit	0.0000	0.0016	0.0016	0.0051	0.0051